analytical chemistry

pubs.acs.org/ac

Review

Analyzing Fundamental Properties of Two-Dimensional Materials by Raman Spectroscopy from Microscale to Nanoscale

Heng Wu, Miao-Ling Lin, Yan Zhou, Xin Zhang, and Ping-Heng Tan*

Cite This: *Anal. Chem.* 2023, 95, 10821−10838

Read Online

ACCESS | Metrics & More | Article Recommendations

CONTENTS

Two-dimensional layered materials consist of chemically bonded monolayers with weak van der Waals (vdW) forces that couple adjacent layers, enabling the preparation of few layers and even monolayers. Monolayer graphene, as the first discovered two-dimensional material (2DM), is a typical semimetal with numerous excellent physical properties, such as zero band gap, high carrier mobility, high thermal conductivity, and high mechanical strength, which have stimulated continuous research.[1] Using the mechanical exfoliation method for preparing monolayer graphene, monolayer semiconductor transition metal dichalcogenides (TMDs), e.g., MoS_2, was successfully realized.[2,3] Various peculiar physical properties such as the direct band gap of the monolayers, rich excitonic effects, and valley polarization properties make TMDs promising for a wide range of novel device applications.[4,5] Beyond the graphene and TMDs whose structures are in-plane isotropic, another class of low-symmetry 2DMs with in-plane anisotropy has attracted more and more interest due to the additional tunability of the in-plane degree of freedom. The first in-plane anisotropic 2DMs ever discovered, black phosphorus (BP), has demonstrated significant variations in many physical properties along its different in-plane crystal axes, making it a fascinating material for further investigation.[6−8] With the development of synthesis techniques, more 2DMs with various electrical properties have been gradually discovered, including insulators (hBN[9]), superconductors ($NbSe_2$, FeSe[10,11]), and topological insulators (Bi_2Se_3, Bi_2Te_3[12]). Moreover, magnetic 2DMs, such as metal phosphorus−sulfur compounds MPS_3 (M = Fe, Mn, Ni), metal halides MX_n (M = Fe, Cr, Ni; X = Cl, Br, I), and $MnBi_2Te_4$,[13] have recently raised new research interest due to their intrinsic long-range magnetic order and layer-dependent magnetic properties.[14] These unique physical properties make 2DMs strong candidates for next-generation electronic, optoelectronic, and energy storage devices.[15]

The ultrathin nature of 2DMs makes their electronic structure, phonon dispersion, and electron−phonon coupling sensitive to the changes in their structure and the external environments, for example, the number of layers, defects, strain, doping, etc.[16] All these aspects have provided a strong basis for the multi-dimensional manipulation of their properties. The atomically flat interfaces of 2DMs without dangling bonds also facilitate the fabrication of vdW heterostructures (vdWHs). Unlike the conventional heterostructures, vdWHs are not constrained by strict lattice matching and can be stacked with different orders and twist angles, thus enabling more functional devices with novel emerging properties.[17,18] Understanding the properties of 2DMs in their intrinsic states, under different external perturbations and even in vdWHs, are essential for materials synthesis, fundamental research, and device applications. Therefore, versatile characterization techniques are required to identify and characterize various types of 2DMs.

Among those various techniques that have been used to characterize the properties of 2DMs, Raman spectroscopy is highly favored by researchers due to its advantages as a fast and non-destructive analytical technique, which is still under

Published: July 10, 2023

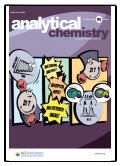

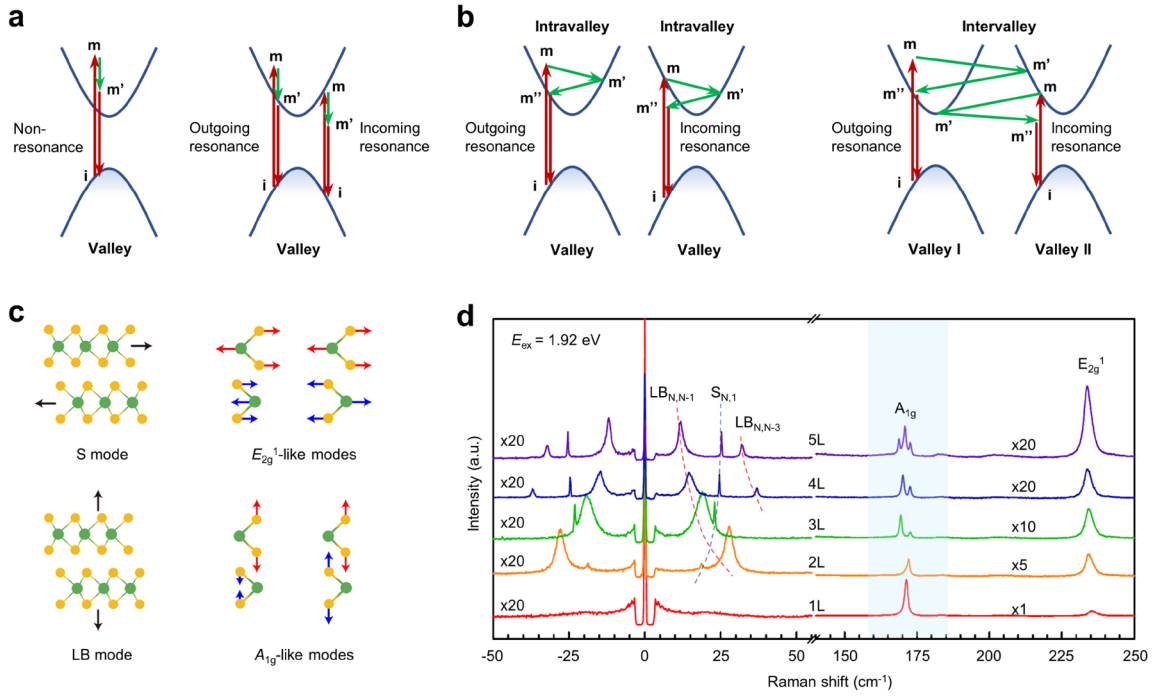

Figure 1. (a) First-order Raman scattering process. The cases of nonresonance, outgoing resonance, and incoming resonance are illustrated. (b) Second-order Raman scattering process. The cases of outgoing resonance and incoming resonance in both intravalley and intervalley scattering are illustrated. (c) The atomic displacements of S, LB, A_{1g}-like, and E_{2g}^1-like modes in multilayer 2H-TMDs. The interlayer coupling makes A_{1g}-like and E_{2g}^1-like modes exhibit different frequencies, i.e., Davydov splitting. (d) Raman spectra of 1−5L 2H-$MoTe_2$. The spectra are scaled and shifted for clarity. Dashed lines are guides for the eye for the frequency trends of the S, LB modes. The light blue region indicates the Davydov splitting of the A_{1g} mode.

progressive improvements for higher optical sensitivity and spatial resolution. By analyzing the peak position, intensity, linewidth, and lineshape of Raman peaks, researchers can obtain basic information about lattice vibrations, electronic structures, and electron−phonon coupling in 2DMs[19]. Changes in phonon dispersion and electronic structure caused by external factors can lead to variations in the Raman spectra of 2DMs relative to the intrinsic Raman features[16]. Therefore, Raman spectroscopy can also characterize the effects of modification on the properties of 2DMs by external factors. To date, several unique Raman spectroscopy techniques have been developed to study the properties of 2DMs from microscale to nanoscale perspectives. As a commonly used one, polarized Raman spectroscopy implemented by combining micro-Raman spectroscopy with polarization optical modules can not only be used to distinguish Raman modes that possess different symmetries but also to obtain rich crystal structure information.[20,21] The development of a single monochromator equipped with notch filters based on volume Bragg gratings has greatly facilitated Raman studies in the low-frequency range, providing a powerful means to effectively detect the unique interlayer lattice vibrations and characterize the number of layers of 2DMs.[22−24] Moreover, Raman spectroscopy based on plasmon-enhanced effects including surface-enhanced Raman spectroscopy, shell-isolated nanoparticle-enhanced Raman spectroscopy, and tip-enhanced Raman spectroscopy (TERS) can dramatically enhance the weak Raman signals, demonstrating an ultra-high chemical sensitivity.[25,26] In particular, TERS can realize the characterization of single molecules and nanostructures through the enhancement effect of highly localized electromagnetic fields at the tip to achieve an ultra-high resolution beyond the optical diffraction limit.[27] This technique has also been gradually used to characterize nanostructures of 2DMs in order to understand the related physical properties at nanoscale.

In this review, we start with an overview of the basic principles of Raman scattering and typical Raman features of 2DMs. Then we introduce the commonly used Raman spectroscopy techniques for studying the fundamental properties of 2DMs and related vdWHs. Furthermore, we reviewed the basic analysis ideas and recent advances of Raman spectroscopy in the characterization of widely concerned properties of 2DMs and vdWHs, including crystalline anisotropy, structural defects, interlayer coupling, exciton−phonon interaction, as well as the effects of the most common external perturbations such as strain and doping. Particularly, we point out that some of the properties can be better revealed at nanoscale via advanced Raman techniques with higher spatial resolution. Finally, we conclude this review with an outlook on the future study of 2DMs and vdWHs by Raman spectroscopy.

OVERVIEW OF RAMAN SPECTROSCOPY IN 2DMS

Raman Scattering Principle. Raman scattering is an inelastic scattering of light that results from the interaction between light and the rotation/vibration modes of molecules or (quasi)particles in solids. The most common type of Raman scattering occurs when light scatters inelastically from lattice vibrations (i.e., phonons).

Raman scattering can be categorized as either first- or higher-order, with the former involving one scattering process of a phonon and the latter involving multiple scattering processes of phonons and/or defects. First-order Raman

https://doi.org/10.1021/acs.analchem.3c00272
Anal. Chem. 2023, 95, 10821−10838

scattering is the most common feature of solids, which involves optical phonons with zero wavevectors ($\mathbf{q} = 0$). For simplicity, we discuss the process that releases a phonon, i.e., the Stokes process. The incident light can excite an electron from the initial state i in the valence band into the intermediate state m, leaving a hole behind. The excited electron at state m can be scattered by a phonon with $\mathbf{q} = 0$ into intermediate state m'. Finally, the electron at state m' and the hole at state i recombine and emit a photon. Depending on whether m and m' are real electronic states, first-order Raman scattering can be further divided into resonant and nonresonant Raman scattering: (i) neither m nor m' is a real electronic state, called nonresonance; (ii) m is a real electronic state, called incoming resonance; (iii) m' is a real electronic state, known as the outgoing resonance (Figure1a). The processes of second- and higher-order Raman scatterings are more complicated. Taking the second-order Raman scattering as an example, the incident light first excites an electron from the valence band state i into an intermediate state m and leaves a hole behind. Then, the electron at state m interacts with a phonon with $\mathbf{q} \neq 0$ into intermediate state m'. Next, the electron at intermediate state m' is scattered by another phonon with $-\mathbf{q}$ into intermediate state m''. Finally, the electron at intermediate state m'' recombines with the hole at state i and emits a photon. Due to the increased number of intermediate states, second-order Raman scattering can hardly occur when none of the intermediate states are real electronic states. When some of the intermediate states are real, i.e., when resonant Raman scattering happens, the scattering probability is greatly enhanced. Similar to the resonant case of first-order Raman scattering, there are incoming and outgoing resonances in second-order Raman scattering. In addition, when the intermediate states m and m' are not in the same energy valley, the corresponding scattering process is called intervalley scattering (Figure 1b). It is important to note that defects and impurities can act as scattering centers to elastically scatter electrons at the intermediate states, providing momentum compensation in this Raman scattering process simultaneously. In this case, the electron is only scattered by one phonon in second-order Raman scattering. In general, the first-order Raman peak exhibits a Lorentzian line shape, while the second- and higher-order Raman modes are usually broader and have weaker intensities. Since the momentum and energy of phonons involved in higher-order Raman scattering depend on the incident photon energy due to conservation laws, the frequencies of higher-order Raman peaks may shift with the excitation energy.[28]

With the dipole approximation, the intensity of the first-order Raman mode is proved to be related to the polarization states of the incident light ($\mathbf{e}_i$) and the collected scattered light ($\mathbf{e}_s$) at the scattering site inside the crystals, which is known as the Raman selection rule.[29] Specifically, Raman intensity I is proportional to

$$I \propto \sum_j |\mathbf{e}_i \cdot \mathbf{R}_j \cdot \mathbf{e}_s|^2 \quad (1)$$

where $\mathbf{R}_j$ is the jth Raman tensor (third-order tensor) of the phonon and can be determined by the symmetry of both crystal structures and vibration modes.[29,30] The selection rule depends on the scattering geometry, which can be denoted as $\mathbf{k}_i(\mathbf{e}_i, \mathbf{e}_s)\mathbf{k}_s$. Here, $\mathbf{k}_i$ and $\mathbf{k}_s$ represent the directions of the incident and scattered photons, respectively.

Lattice Vibrations in 2DMs. The first-order intralayer Raman modes are determined by the crystal symmetry of 2DMs. For example, the point group of monolayer TMDs in the 2H phase (i.e., 2H-TMD) is D_{3h}, and the irreducible representations of the phonon modes at the Γ point of the Brillouin zone are $\Gamma = A_1' + 2A_2'' + 2E' + E''$. One A_2'' mode and one doubly degenerate E' mode belong to acoustic modes. Another A_2'' mode is infrared active; A_1' and E'' modes are Raman active; and one E' mode is both Raman and infrared active. The irreducible representations of phonon modes with similar atomic displacements vary with different numbers of layers due to the different point group symmetry of the corresponding TMD flakes. A_1' and E' modes of the monolayer 2H-TMDs correspond to A_{1g} and E^1_{2g} modes of the bulk counterpart, respectively.[31] In this review, we use A_{1g}, E^1_{2g} modes of bulk 2H-TMDs to denote the corresponding modes of multilayer 2H-TMDs for convenience.

The interaction between rigid layers of multilayer 2DMs leads to their phonon dispersion being slightly different from that of monolayer 2DMs and the emergence of new intralayer vibrational modes in comparison to those of monolayer 2DMs. This effect is known as Davydov splitting (Figure 1c). However, the frequency difference of these modes is usually small due to the weaker interlayer interaction relative to the intralayer chemical bonding.[32−35] Interlayer coupling can also affect the electronic structure of 2DMs, resulting in variations in Raman features observed in resonance Raman spectroscopy. The 2D mode of graphene flakes provides a prime example, as it involves double resonance Raman scattering of iTO phonons near the K point of the Brillouin zone. This mode is highly sensitive to any changes in the electronic structure. In multilayer graphene, the electronic band undergoes significant evolution as the number of layers increases. Consequently, the 2D mode in such systems involves multiple nonequivalent double resonance Raman scattering processes, leading to a superposition of several Lorentzian peaks that causes a noticeable alteration in the line shape of the 2D mode.[36]

The van der Waals interaction between rigid layers of multilayer 2DMs results in the relative vibration between the layers and the emergence of another important type of Raman mode, namely, the interlayer vibration mode, which is absent in monolayer 2DMs. According to the layer vibration direction, the interlayer modes can be further divided into in-plane shear (S) modes and out-of-plane layer-breathing (LB) modes (Figure 1c). The S mode has also been referred to as the C mode since it provides a direct measurement of the interlayer *coupling*.[22] The frequencies of S and LB modes are typically below 100 cm^{-1} due to the weak interlayer vdW interaction and show a significant dependence on the number of layers of 2DMs.[24] There are $(N - 1)$ degenerate S modes and $(N - 1)$ LB modes in the in-plane isotropic 2DMs of N-layers (NL), and they can be respectively denoted as $S_{N,N-j}$ and $LB_{N,N-j}$ (j = 1, 2, ..., $N - 1$) where the $S_{N,1}$ ($LB_{N,1}$) shows the highest frequency. These interlayer modes can be described by the linear chain model (LCM),[22,23] in which each rigid layer is considered as a ball connected by van der Waals force as there is no relative motion of atoms within the rigid layer. For 2DMs with a number of layers of N (NL), the frequencies of interlayer modes can be expressed analytically as

https://doi.org/10.1021/acs.analchem.3c00272
Anal. Chem. 2023, 95, 10821−10838

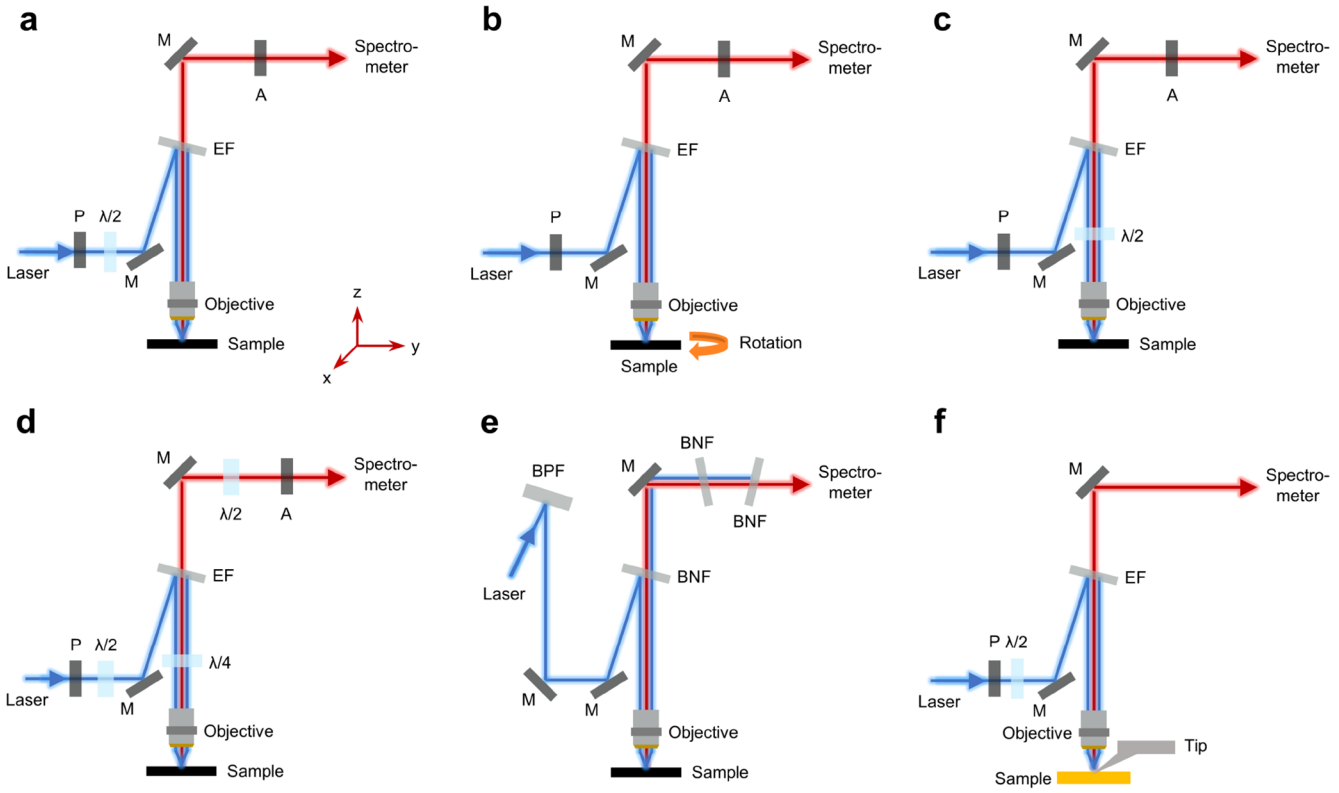

Figure 2. Schematics of the setups of typical Raman spectroscopy. (a–c) ARPR Raman spectroscopy. (d) Circularly polarized Raman spectroscopy. (e) Low-frequency Raman spectroscopy. (c) TERS. The laboratory coordinate (xyz) is illustrated. M, mirror; P, polarizer; A, analyzer; $\lambda/2$, half-wave plate; $\lambda/4$, quarter-wave plate; EF, edge filter; BPF, VBG-based bandpass filter; BNF, VBG-based notch filter.

$$\omega\left(\mathrm{S}_{N,N-j}\right) = \sqrt{\alpha^{\parallel}/\pi c^2 \mu}\,\sin(j\pi/2N)$$
$$\omega\left(\mathrm{LB}_{N,N-j}\right) = \sqrt{\alpha^{\perp}/\pi c^2 \mu}\,\sin(j\pi/2N), \quad (2)$$

where $c = 3 \times 10^8$ m·s^{-1} is the speed of light and μ is the mass per unit area of a single layer. $\alpha^{\parallel}$ and $\alpha^{\perp}$ are the nearest-neighbor force constants of in-plane and out-of-plane interlayer coupling, respectively.[22,23] Until now, the interlayer mode frequencies of common 2DMs including hBN,[37] TMDs,[23,38] BP,[39] ReS_2, and $ReSe_2$[40,41] have been well explained by LCM, where only the nearest-neighbor interactions are involved. On the other hand, the next-nearest-neighbor LB force constants should be considered in reproducing the LB mode frequencies of multilayer graphene.[42]

Finally, as a specific example, Figure 1d depicts the Raman spectra of 1–5L $MoTe_2$ with an excitation energy of 1.92 eV. The first-order Raman modes including intralayer A_{1g}, E^1_{2g} modes, and interlayer S, LB modes are shown. The S and LB modes exhibit layer-dependent frequencies, and the Davydov splitting of A_{1g} can also be clearly observed.

TYPICAL RAMAN SPECTROSCOPY TECHNIQUES FOR 2DMS

Polarized Raman Spectroscopy. Polarized Raman spectroscopy based on the Raman selection rules is a powerful analytical tool that provides insight into the intensity response of Raman modes in a specific scattering geometry to the polarization states of incident and scattered light.

For linearly polarized Raman spectroscopy, the incident and scattered light are, respectively, along the $-z$ and z directions in backscattering geometry, and their polarization direction is in the xy-plane. The polarization vectors can be represented as $\mathbf{e}_i = (\cos\theta_i, \sin\theta_i, 0)$ and $\mathbf{e}_s = (\cos\theta_s, \sin\theta_s, 0)$, where θ_i and θ_s are the angles of incident and scattered light with respect to the x direction, respectively. The simplest linearly polarized Raman configurations are parallel- and cross-polarization configurations. In the parallel polarization configuration, both θ_i and θ_s are set to 0° or 90° by a polarizer and an analyzer, i.e., the polarization of the incident and scattered light is along the x or y direction, which is usually denoted as $\bar{z}(xx)z$ or $\bar{z}(yy)z$, respectively. In the latter, θ_i (θ_s) is set to 0° (90°) or 90° (0°), which can be denoted as $\bar{z}(xy)z$ or $\bar{z}(yx)z$, respectively. Since only the intensity response of Raman modes to the specific polarization states of the incident and scattered light is obtained, these two configurations are commonly used to distinguish Raman modes with different symmetries. In order to obtain comprehensive information about the crystal symmetry, angle-resolved polarized Raman (ARPR) technique is developed. To perform ARPR measurement, a polarizer and an analyzer are usually used to set the polarization states of the incident beam from a laser and scattered light before the spectrometer entrance to the x (y) axis of the laboratory coordinate, respectively. Depending on whether the half-wave plate is used and the sample is rotated, there are three typical angle-resolved polarization configurations:[43] (i) using a half-wave plate to change θ_i of $\mathbf{e}_i$, and $\mathbf{e}_s$ is fixed by the analyzer, as shown in Figure 2a; (ii) rotating the sample while fixing $\mathbf{e}_i$ and $\mathbf{e}_s$ to the x- or y-axis of the laboratory coordinate, as depicted in Figure 2b; in this case, the Raman tensor is dependent on the rotation angle in the laboratory coordinate; (iii) inserting a half-wave plate into the common optical path of the incident

https://doi.org/10.1021/acs.analchem.3c00272
Anal. Chem. 2023, 95, 10821–10838

laser and scattered Raman signal between objective and Raman filter to simultaneously vary $\mathbf{e}_i$ and $\mathbf{e}_s$, as illustrated in Figure 2c. The last two configurations are equivalent to each other for ARPR results. More discussion about the three configurations can be found in ref 43. With the help of ARPR spectroscopy, detailed information on matrix elements of Raman tensors can be obtained based on the Raman selection rule, and the orientation of crystal axes can be determined due to the fact that the maximum/minimum response of a specific mode is usually along the crystal axes.

Recently, polarized Raman experiments with circularly polarized light have attracted wide attention. To generate circularly polarized light, a quarter-wave plate is needed. The typical configuration is illustrated in Figure 2d.[44] The polarization of incident (scattered) light is $\sigma+$ or $\sigma-$, and the corresponding $\mathbf{e}_i$ ($\mathbf{e}_s$) are $(1, i, 0)/\sqrt{2}$ or $(1, -i, 0)/\sqrt{2}$, respectively. Four polarization configurations are further determined, including ($\sigma+$ $\sigma+$), ($\sigma-$ $\sigma-$), ($\sigma+$ $\sigma-$), and ($\sigma-$ $\sigma+$). Analogous to the parallel- and cross-polarization configuration, the circularly polarized Raman spectroscopy follows the Raman selection rules and is also commonly used for Raman mode identification in 2DMs with hexagonal lattices.[44]

Low-Frequency Raman Spectroscopy. The typical range for measuring Raman spectra is above 100 cm^{-1} for a common single monochromator using a notch or edge filter. However, informative signals can still exist in the range below 100 cm^{-1}, which include the Raman signals of the interlayer vibration modes for multilayer 2DMs. Detecting these modes with a conventional single monochromator is challenging since they closely approach the Rayleigh line. In the past, double or triple cascaded high-resolution monochromators were used to access low-frequency Raman signals, but these setups have low throughput and long accumulation time is necessary.[38,45,46] Recent developments in volume Bragg grating (VBG) based notch filters (BNF) have greatly improved the efficiency of detecting low-frequency Raman modes when combined with single-grating Raman spectrometers.[22,23] Each BNF typically has a narrow bandwidth (~5−10 cm^{-1}) and high transmittance (up to 80−90% depending on the laser wavelength), allowing for a high signal-to-noise ratio with easy operation. Figure 2e presents a schematic diagram of a low-frequency Raman system based on BNFs, where three BNFs with optical density of 3−4 are used to efficiently reflect Rayleigh signals and transmit Raman signals.[22] A VBG-based bandpass filter (BPF) is also used to remove the plasma lines of the laser. This setup can detect Raman modes with frequencies down to 5 cm^{-1} and was used to successfully measure the weak S modes in multilayer graphene,[22] which was the first report of interlayer modes in 2DMs.

Tip-Enhanced Raman Spectroscopy. Micro-Raman spectroscopy has achieved unparalleled success in various applications. However, its submicrometer spatial resolution limits its characterization ability toward the atomic or nanoscale information on 2DMs. TERS, which combines Raman spectroscopy and scanning probe microscopy, is a versatile tool that provides a spatial resolution ranging from several angstroms to tens of nanometers, exceeding the optical diffraction limit.[25,27] Laser excitation at an appropriate wavelength and polarization can generate collective oscillations of the surface electrons of the tip, resulting in localized surface plasmon resonance. Combined with the lightning rod effect of the tip, this produces a strong electromagnetic field, which significantly enhances the Raman signal of the sample below.[26] Figure 2f illustrates a typical TERS configuration with top illumination. In this case, a tilted tip is required to avoid shadow created by the cantilever and a half-wave plate is used to adjust the polarization direction of the incident laser.[47] The electromagnetic enhancement of TERS is affected by several factors, including the incident laser (wavelength, polarization, and incident angle), tip (material, curvature, radius, tip angle, and morphology), substrate (material, roughness, and tip−substrate distance), and the surrounding dielectric environment of the tip.[26] Atomic force microscopy (AFM) combined with Raman spectroscopy allows TERS measurements at ambient temperature and pressure, which can achieve spatial resolution at nanoscale. TERS measurements can also be performed by combining scanning tunneling microscopy (STM) and Raman spectroscopy. This configuration can achieve atomic-level spatial resolution but requires higher measurement conditions simultaneously, i.e., low temperature and ultrahigh vacuum (UHV) environments.[27,47,48] The significant enhancement on the Raman signal and the ultrahigh spatial resolution of TERS make it naturally suitable for probing the nanoscale properties of 2DMs, such as defects and local strain.[48−50]

APPLICATION OF RAMAN SPECTROSCOPY IN ANALYZING FUNDAMENTAL PROPERTIES OF 2DMS

Crystalline Anisotropy. Graphene and 2H-TMD flakes have been widely studied due to their excellent optical and electrical properties, which exhibit high in-plane isotropy (point group of D_{6h}).[51] However, another class of 2DMs with reduced structural symmetry, such as BP (D_{2h}),[6,52] WTe_2 (C_{2v}),[53] GaTe (C_{2h}),[54] and ReS_2 (C_i),[41] exhibits significant difference in electronic structure and phonon dispersion along different crystal axes of the 2D basal plane, i.e., in-plane anisotropy.[51] This property provides an additional degree of freedom to manipulate their optical, electrical, thermal, and mechanical properties, making these 2DMs promising for applications in polarized optical components, polarization sensors, and high-performance transistors.[6,55−60] Identifying the in-plane crystal axes is critical for investigating the in-plane anisotropy and related device applications. Although X-ray diffraction, transmission electron microscopy, and other techniques were commonly used to characterize the crystal structure, Raman spectroscopy has gradually become an important tool for crystal structure identification due to its fast and nondestructive characteristics. The polarization dependence of a Raman mode is determined by the form of its Raman tensor, which is influenced by the crystal symmetry, birefringence, and dichroism along different crystal axes.[61−63] Therefore, polarized Raman spectroscopy can be employed to effectively identify the in-plane anisotropy and crystal axes by correlating the polarization response of the Raman modes to the crystal symmetry.

The in-plane orientation of anisotropic 2DMs can be determined by the ARPR intensity. Due to the birefringence and linear dichroism of an anisotropic crystal, the polarization response of its Raman intensity deviates from the theoretical result given by the Raman selection rule if a complex Raman tensor is not considered.[61] The birefringence causes phase differences when the laser propagates along different principal axis directions, while the linear dichroism leads to anisotropic absorption.[63] A widely adopted approach is introducing a

https://doi.org/10.1021/acs.analchem.3c00272
Anal. Chem. 2023, 95, 10821−10838

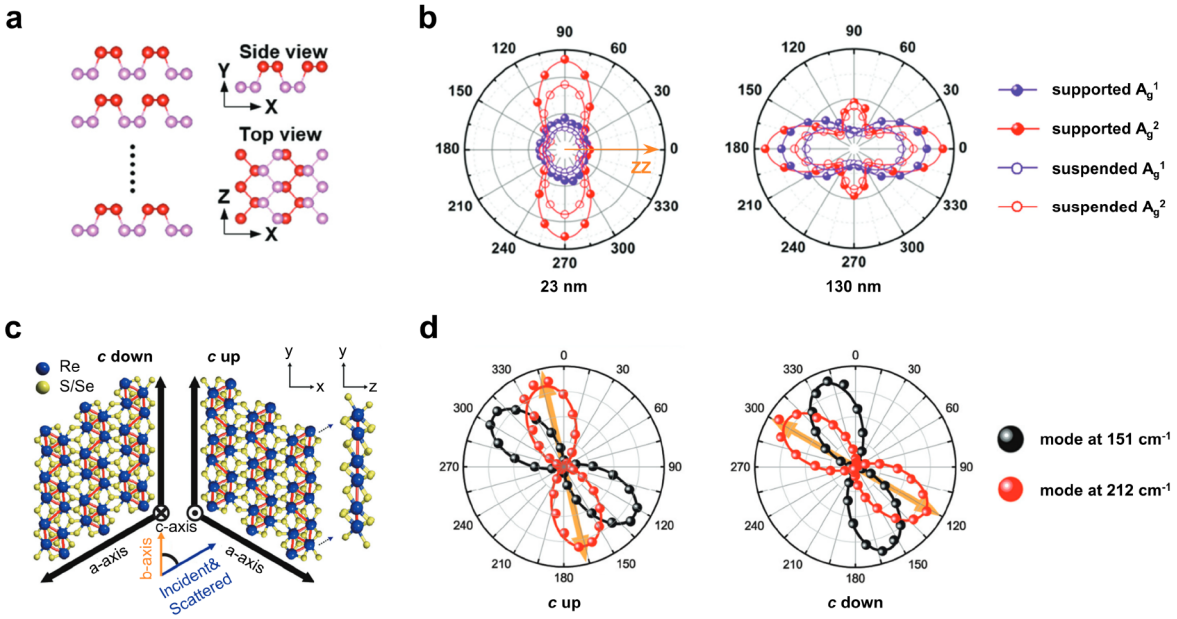

Figure 3. (a) Schematic illustration of orthorhombic BP crystal structure. (b) ARPR responses of A_g^1 and A_g^2 modes collected from both the suspended and supported BP regions of 23 nm and 130 nm by a 532 nm laser. Reproduced from Zou, B.; Wei, Y.; Zhou, Y.; Ke, D.; Zhang, X.; Zhang, M.; Yip, C.; Chen, X.; Li, W.; Sun, H. *Nanoscale Horiz.* **2021**, *6*, 809 (ref 64), with permission of The Royal Society of Chemistry. (c) Top- and side-view of a crystal structure of triclinic 1L-ReX_2. The *c*-up type has the *c*-axis coming out of the plane and the *c*-down type coming into the plane. (d) ARPR responses of Raman modes at 151 cm^{-1} and 212 cm^{-1} of *c*-up and *c*-down type monolayer ReS_2 with an excitation energy of 2.41 eV. The arrows indicate the *b*-axis. Reproduced from Choi, Y.; Kim, K.; Lim, S.; Kim, J.; Park, J.; Kim, J.; Lee, Z.; Cheong, H. *Nanoscale Horiz.* **2020**, *5*, 308 (ref 65), with permission of The Royal Society of Chemistry.

complex Raman tensor in the Raman selection rule to consider birefringence or the linear dichroism effect. This method tends to explain the experimental results well; however, it is impossible to distinguish the respective contributions from birefringence and linear dichroism effects. The treatment based on complex Raman tensors has been used to explain the polarization response and to determine the crystal axes of anisotropic 2DMs with specific thicknesses, such as BP,[61,62] 1T′-$MoTe_2$,[66] 1T′-WTe_2,[53] ReS_2, and $ReSe_2$.[65] In the practical application, the identification of the crystal orientation of anisotropic 2DMs based on a complex Raman tensor typically requires the information on the excitation energy, sample thickness, and the dielectric layers of the underlying substrate because the polarized Raman spectra are also affected by the interference effects in the multilayered structures consisting of air, sample, and substrate.[62,63] For example, the intensity maximum of A_g^1 and A_g^2 modes in bulk BP is along either *a*- (zigzag, ZZ) or *b*- (armchair, AC) axis; however, that in a BP flake has been proven to be changed with its thicknesses (Figure 3a,b).[62,64] Thus, the factors discussed above make it difficult to identify the crystal axes of anisotropic 2DM flakes at arbitrary thicknesses. However, the intensity ratio between A_g^1 and A_g^2 modes can be used to determine the crystal axes of BP flakes. Zou et al. investigated the ARPR intensity of A_g^1 and A_g^2 modes of BP flakes with thicknesses ranging from 8 nm to 170 nm with the excitation wavelength of 532 nm, 633 nm, and 785 nm.[64] The intensity of A_{1g}^1 mode along the ZZ axis ($I_{A_g^1}^{ZZ}$), AC axis ($I_{A_g^1}^{AC}$), and A_g^2 mode along the ZZ axis ($I_{A_g^2}^{ZZ}$), AC axis ($I_{A_g^2}^{AC}$) was found to satisfy the relationship $I_{A_g^2}^{AC}/I_{A_g^1}^{AC} > I_{A_g^2}^{ZZ}/I_{A_g^1}^{ZZ}$. This relation can be used as a concise criterion to conveniently identify the ZZ and AC directions of BP for arbitrary thicknesses.

In addition to the in-plane axes, it should also be noted that the out-of-plane *c*-axis of triclinic 2DMs such as ReX_2 (X = S, Se) is nonorthogonal to the *a*- and *b*-axes (Figure 3c). Choi et al. developed an unambiguous method to determine both the in-plane and out-of-plane axes of few-layer ReS_2 and $ReSe_2$ by polarized Raman spectroscopy. During the ARPR measurement, the exfoliated ReS_2 and $ReSe_2$ flakes were placed on a transparent quartz substrate with *c*-axis both up and down by flipping the sample over.[65] Under the excitation energy of 2.33 eV, the polar plots for modes at 151 cm^{-1} and 212 cm^{-1} with the *c*-axis up and the *c*-axis down show obvious mirror symmetry (Figure 3d). A similar trend between modes at 124 cm^{-1} and 160 cm^{-1} of $ReSe_2$ samples was also observed under the excitation energy of 1.96 eV. Combined with the results of high-resolution scanning transmission electron microscopy, the orientation of the *c*-axis of ReX_2 (X = S, Se) can be determined by the relative rotation of the maximum intensity polarization directions of the certain two modes in polar plots with specific excitation energies.

Structural Defects. The morphological characteristics of 2DMs with large specific surface area make it inevitable to introduce defects during growth and mechanical processing, including vacancies, wrinkles, and edges. Defects can have a significant impact on the physical and chemical properties of 2DMs. For example, defects can introduce additional electronic states and lead to specific optical processes; defect−carrier and defect−phonon scattering can affect the electrical transport and thermal properties; defects can also act as active sites to enhance the catalytic properties of 2DMs.[68−70] Therefore, characterizing the defect structure along with the defect-induced properties of 2DMs is important to improve the performance of relevant devices.

https://doi.org/10.1021/acs.analchem.3c00272
Anal. Chem. 2023, 95, 10821−10838

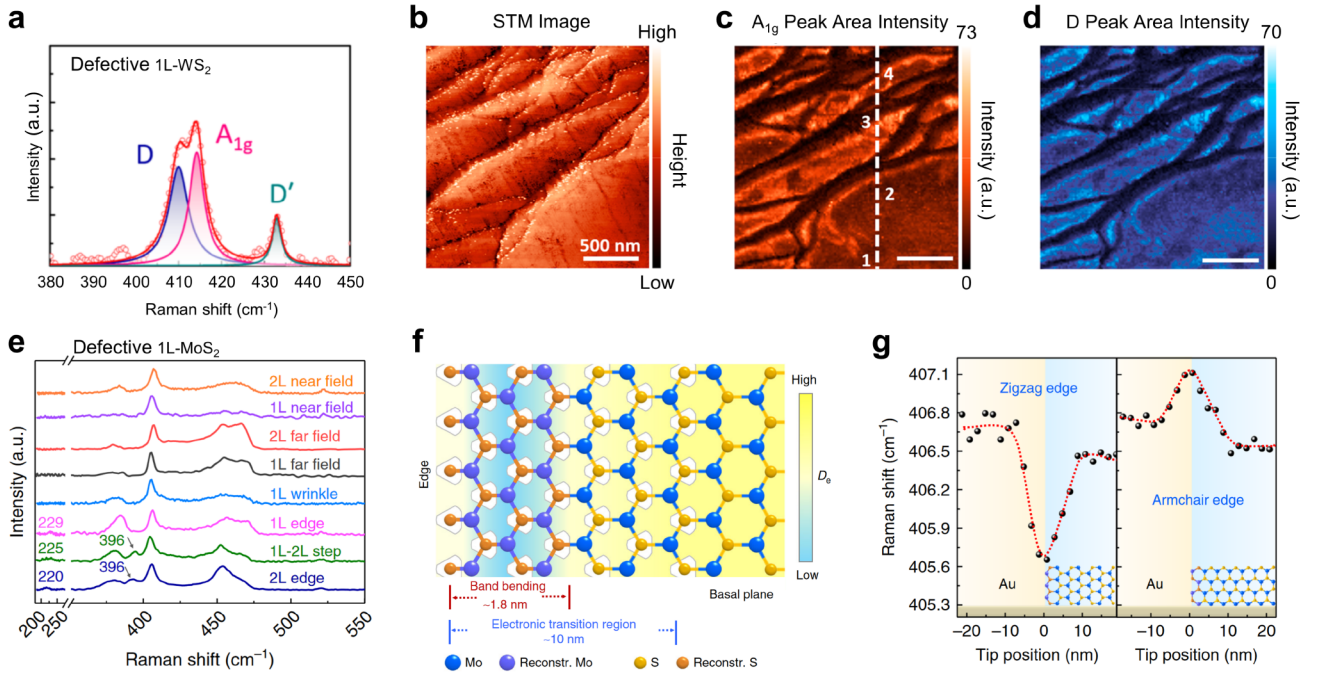

Figure 4. (a) TERS spectra of the defective 1L-WS_2. The D and D′ peaks are defect-induced Raman peaks. (b) STM image and TERS image of (c) A_{1g} and (d) D peak area intensity. Reproduced from Lee, C.; Jeong, B.; Yun, S.; Lee, Y.; Lee, S.; Jeong, M. *ACS Nano.* **2018**, *12*, 9982−9990 (ref 67). Copyright 2018 American Chemical Society. (e) Raman spectra of four types of one-dimensional defects and the basal plane in MoS_2 when the tip was approached and retracted. (f) Schematic diagram of band reconstruction and electronic transition region of MoS_2 near the edge. D_e is the electron density. (g) The peak position of the A_{1g} mode across a zigzag edge and an armchair edge (shown in the insets). Reprinted by permission from Macmillan Publishers Ltd.: Huang, T.; Cong, X.; Wu, S.; Lin, K.; Yao, X.; He, Y.; Wu, J.; Bao, Y.; Huang, S.; Wang, X.; Tan, P.; Ren, B. *Nat. Commun.* **2019**, *10*, 5544 (ref 50). Copyright 2019.

As a fingerprint of the material structure, the Raman spectroscopy of 2DMs is also sensitive to the presence of defects. The destruction of the complete crystal structure by defects directly leads to Raman intensity attenuation, frequency shift and (asymmetric) broadening of the first-order phonon modes, as well as the emergence of new Raman modes.[71−74] The analysis of the Raman spectra of defective 2DMs can yield a wealth of information related to the defects. First, the disruption of lattice integrity by defects leads to a decrease in the intensity of the intrinsic Raman modes of 2DMs, which can be interpreted as a decrease in the area of the intrinsic sample in the test region. For example, the intensity of the G mode in graphene decreases with increasing concentration of defects.[71] The alteration of Raman mode intensity in 2DMs by defects is directly related to the defect concentration, which is manifested by the average distance between defects.[75] The exact relationship needs to be modeled and analyzed for different defect types (e.g., point defects, line defects).[71,72,75,76] Second, the space translation symmetry breaking by defects results in the relaxation of momentum-conservation in Raman scattering, leading to frequency shifts and broadening of the intrinsic first-order Raman modes. The motion of phonons can be described by Bloch wave packets whose uncertainties of wave vectors ($\Delta\mathbf{q}$) and position ($\Delta\mathbf{x}$) satisfy the uncertainty relation. In perfect crystals, phonons can exist at any position in the crystal, so the $\Delta\mathbf{x}$ is infinite; that is, the wave vector is uniquely determined. In crystals with defects, the $\Delta\mathbf{x}$ becomes finite, so the $\Delta\mathbf{q}$ is nonzero, indicating that phonons away from the center of the Brillouin zone are involved in Raman scattering. Thus, the observed first-order Raman modes of defective 2DMs are in fact a superposition of contributions from phonons with different wavevectors, whose frequencies and line widths significantly change in comparison to those of perfect crystals. The phenomena can be analyzed in detail by the phonon confinement model originally proposed by Richter, Wang, and Ley (usually referred as the RWL model),[77] which has been applied to explain the evolution behavior of first-order Raman modes of defective 2DMs with respect to the defect concentration, including graphene,[71] TMDs,[72,73] and BP[74] flakes. Third, defects also serve as scattering centers to activate new Raman modes by resonance Raman scattering. The activation of D and D′ modes in defective graphene is a typical example of the involvement of defects as scattering centers in the double resonance Raman process due to the peculiar band structure of graphene.[78] Defects provide momentum compensation for the involved electrons to make the momentum conservation be satisfied in the Raman process.[16,79]

Micro-Raman spectroscopy can quickly extract the basic properties of point defects with a high concentration. However, when 2DMs have a low concentration of point defects, micro-Raman spectroscopy is no longer applicable for detailed investigation because defect-induced Raman modes may exhibit a weak intensity with such a low signal-to-noise ratio that they are not observable. Other types of defects cannot be well distinguished by micro-Raman spectroscopy due to its submicrometer spatial resolution. As an advanced Raman spectroscopy technique, TERS exhibits huge intensity enhancement and ultrahigh spatial resolution, making it possible to study the concentration and type of defects at the nanometer scale.

https://doi.org/10.1021/acs.analchem.3c00272
Anal. Chem. 2023, 95, 10821−10838

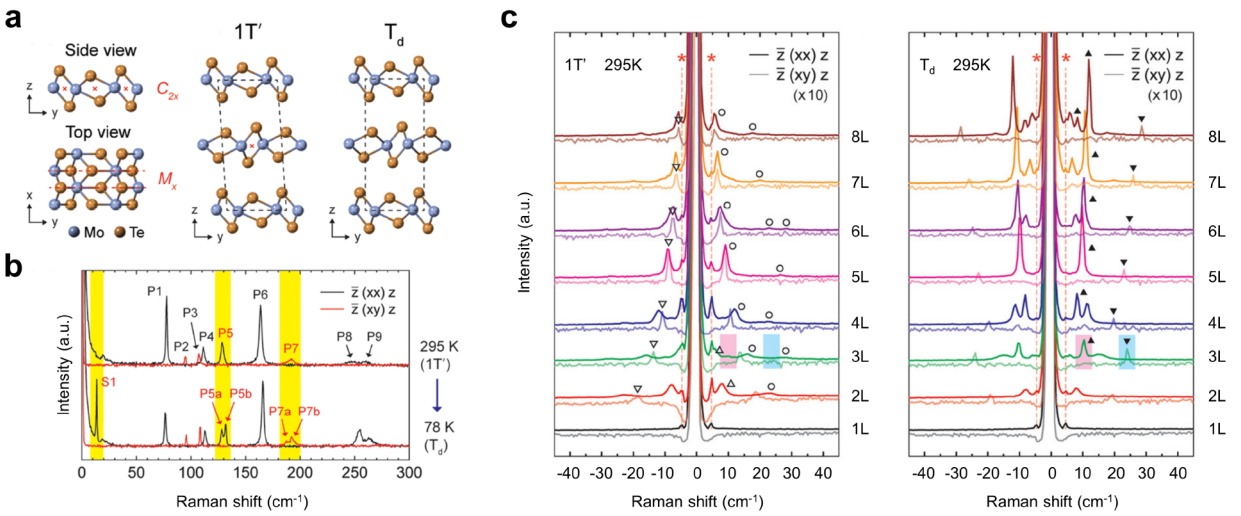

Figure 5. (a) Crystal structure of 1T′- and T_d-$MoTe_2$. (b) Polarized Raman spectra of bulk 1T′-$MoTe_2$ at 295 and 78 K after phase transition to the T_d phase. The Raman signatures of structural phase transition are highlighted in yellow. (c) Polarized Raman spectra of 1−8L $MoTe_2$ in the 1T′ phase and T_d phase. The S and LB modes are indicated by hollow triangles and circles, respectively. Extra Raman modes in the T_d phase are indicated by solid triangles. Reproduced from Cheon, Y.; Lim, S.; Kim, K; Cheong, H. *ACS Nano* 2021 15 (2), 2962−2970 (ref 100). Copyright 2021 American Chemical Society.

TERS mapping was first applied to the characterization of defects in monolayer graphene, including the defect distribution,[80] phase-breaking lengths of the graphene edge,[81] and the average distance between point defects.[82] Subsequently, this technique was further used to characterize the surface defects of other 2DMs. Lee et al. found that defect-induced A_{1g} mode redshift in 1L-WS_2, as well as the activation of D and D′ modes on its sides (Figure 4a).[67] They excluded the strain effects and attributed the cause of these phenomena to the formation of sulfur vacancies in combination with theoretical calculations. The TERS mapping of the frequency and intensity of the A_{1g}, D, and D′ modes illustrates a complete defect distribution on the WS_2 surface, which is in agreement with the results of STM (Figure 4b−d). Analogously, Kato et al. performed TERS mapping of the A_{1g} mode intensity of 1L-MoS_2 in the wrinkled region, which successfully captured high-resolution (∼20 nm) images of the wrinkles and matched well with the morphological images obtained by AFM.[83]

The electronic properties of surface defects in 2DMs can also be spatially resolved by TERS, and the effect of the defects on the physical properties of the surrounding pristine material can be determined simultaneously. Huang et al. performed the AFM-based TERS measurements of different line defects in 1−2L MoS_2 (Figure 4e) and claimed that edge-induced bending of electronic band structure can activate double resonance Raman scattering of the LA(M)+TA(M) mode, whose intensity can be used to determine the corresponding energy band-bending region.[50] Meanwhile, frequency shifts of the doping-sensitive A_{1g} mode at different edge points reveal the electron density distribution nearby. Combining theoretical calculations and TERS line mapping of the LA(M)+TA(M) and A_{1g} modes, the length of the transition region between intrinsic MoS_2 and the edge is determined (Figure 4f). In addition, different edge types such as zigzag and armchair edges can also be identified by the variation of the A_{1g} mode frequency (Figure 4g), which will play an important role in the practical application of MoS_2.

Interlayer Coupling. Multilayer 2DMs are composed of rigid layers that are naturally bonded by vdW forces, and these weak interactions create opportunities to construct 2DMs with different stacking configurations, both natural and artificial. Different stacking structures can modify the interlayer coupling and affect their optical, electrical, and vibrational properties.[84−87] For vibrational properties, interlayer coupling directly leads to the emergence of layer-dependent interlayer S and LB modes in multilayer 2DMs, which are exceptionally sensitive to the interface environment. The detection of interlayer modes using low-frequency Raman spectroscopy not only allows precise characterization of the number of layers and stacking configuration of 2DMs but also obtains information about interlayer coupling of 2DMs and related vdWHs.[24]

The clear observation of interlayer modes is a prerequisite to evaluate interlayer coupling in 2DMs and vdWHs. However, the Raman intensity of the interlayer modes is usually weak. Selecting an appropriate excitation energy to match the resonance condition can significantly improve the Raman intensity of 2DMs and vdWHs. For instance, interlayer modes of twisted multilayer graphene can be dramatically enhanced by matching the excitation energy with the energy between the conduction and valence band van Hove singularities.[42,88,89] Similarly, a resonant excitation that matches a specific excitonic state in BP, TMDs, and related vdWHs can also make the interlayer modes be enhanced and easily observed.[34,39,90−95]

2DMs with different stacking phases exhibit different structural symmetry, interlayer coupling, and polarizability, which lead to striking variations in the relative Raman intensity of interlayer modes, as observed in AB/ABC-stacked multilayer graphene[96] and 2H/3R-stacked TMDs.[41,97] The relative intensity of the corresponding interlayer modes can be well explained by the interlayer bond polarizability model, which treats each layer as a single object with no need of intralayer structural details, so only the interlayer bond vectors and polarizabilities are required to determine Raman intensities of both S and LB modes.[98,99] A recent work by Cheon et al. identified the phase transition from the monoclinic 1T′ to the orthogonal T_d phases of $MoTe_2$ and analyzed the corresponding interlayer coupling.[100] The 1T′ and T_d phases differ only slightly in stacking along the *c*-axis direction (Figure 5a).

https://doi.org/10.1021/acs.analchem.3c00272
Anal. Chem. 2023, 95, 10821−10838

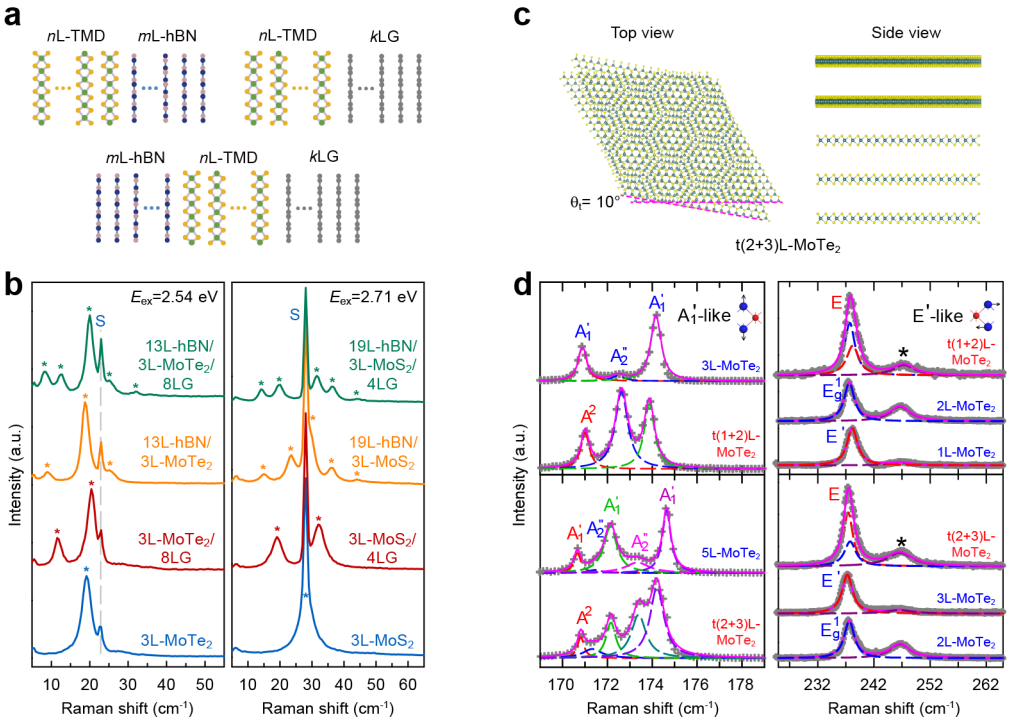

Figure 6. (a)Schematics of *n*L-TMD/*m*L-hBN, *n*L-TMD/*k*LG binary vdWHs and *m*L-hBN/*n*L-TMD/*k*LG ternary vdWHs. (b) Low-frequency Raman spectra of 13L-hBN/3L-$MoTe_2$/8LG, 19L-hBN/3L-MoS_2/4LG, and the corresponding binary hBN/TMD, TMD/graphene vdWHs, and individual TMD flakes. The LB modes are marked by asterisks (*). Reprinted by permission from Macmillan Publishers Ltd.: Wu, H.; Lin, M.; Leng, Y.; Chen, X.; Zhou, Y.; Zhang, J.; Tan, P., *npj 2D Mater. Appl.* **2022**, *6*, 87 (ref 95). Copyright 2012. (c) Schematic of twisted (2 + 3)L-$MoTe_2$ (denoted as t(2 + 3)L-$MoTe_2$) with a twist angle of 10°. (d) Left panel: Raman spectra of A_1'-like modes in t(m + n)L-$MoTe_2$ and the corresponding NL-$MoTe_2$ (N = m + n). Right panel: Raman spectra of E'-like modes in twisted (m + n)L-$MoTe_2$, mL-$MoTe_2$, nL-$MoTe_2$. The gray crosses and dashed lines indicate the spectra data obtained under 671 nm excitation at 4 K and the fitting results, respectively. Reproduced from Leng, Y.; Lin, M.; Zhou, Y.; Wu, J.; Meng, D.; Cong, X.; Li, H.; Tan, P. *Nanoscale* **2021**, *13*, 9732−9739 (ref 35), with permission of The Royal Society of Chemistry.

Polarized Raman spectra of the T_d phase at low temperature exhibit the newly emerged low-frequency mode and the splitting of two high-frequency modes, different from that of the 1T′ phase at room temperature (Figure 5b). The layer-dependent interlayer modes of the two phases also exhibit a pronounced difference in the number of observed modes and in their relative Raman intensities (Figure 5c). The frequencies of observed interlayer modes can be well reproduced by LCM, and similar coupling strengths were claimed for both phases according to their extracted force constants. This further indicates that minor stacking differences between the two phases would not obviously change the interlayer coupling strength of $MoTe_2$.

For vdWHs (including twisted 2DMs), due to the interlayer coupling at the heterointerface (also known as interfacial coupling), the number and peak position of the observed interlayer modes could be significantly different from those of constituents. Indeed, various interlayer modes have been identified in twisted multilayer graphene,[42,88] twisted bilayer TMD,[101−103] and vdWHs.[93,104,105] In vdWHs with large twist angles or large lattice mismatch at heterointerfaces, the S modes are found to be localized in the constituents.[42,88,93,105] In this case, no new S modes can be observed in vdWHs except for those of constituents. However, the non-negligible LB interfacial coupling at the heterointerface of vdWHs leads to the normal displacements of the corresponding LB modes in vdWHs extending throughout the entire heterostructures. After considering the LB interfacial coupling force constant, the frequency of the observed LB modes in vdWHs can also be well understood by LCM.[93,95,105] Conversely, the strength of interfacial coupling in vdWHs can be extracted from the measured LB mode frequencies. For TMD-based vdWHs composed of hBN or graphene (Gr), i.e., Gr/TMDs and hBN/TMDs vdWHs, the LB force constants at the heterointerface are comparable to those of constituents. The method to evaluate the interfacial coupling strength has recently been applied to some new vdWHs such as MoSSe/MoS_2 Janus heterobilayer.[106] The S and LB modes in the MoSSe/MoS_2 heterobilayer exhibited higher frequencies than those in 2L-MoS_2, and the extracted S and LB force constants were about 10% higher than those in the pristine 2L-MoS_2. This increase was attributed to the rearrangement of the atomic configuration of sulfur and selenide atoms and the reduction in Mo−Mo atomic layer spacing. Wu et al. further extended the LCM for ternary vdWHs. In vdWHs composed of Gr, hBN, and TMDs, the interfacial coupling strengths were evaluated via the emergent LB modes enhanced by cross-dimensional electron−phonon coupling.[95] Indeed, due to the presence of interfacial coupling, the observed LB modes in Gr/TMD/hBN and Gr/hBN/TMD vdWHs were significantly different from those of the individual constituents and the corresponding binary vdWHs (Figure 6a).[95]

Interlayer coupling in 2DMs can also modulate the frequency of their intralayer modes, leading to the so-called Davydov splitting.[32−34] Two models have been used to explain such a phenomenon, including the force constant model that

https://doi.org/10.1021/acs.analchem.3c00272
Anal. Chem. 2023, 95, 10821−10838

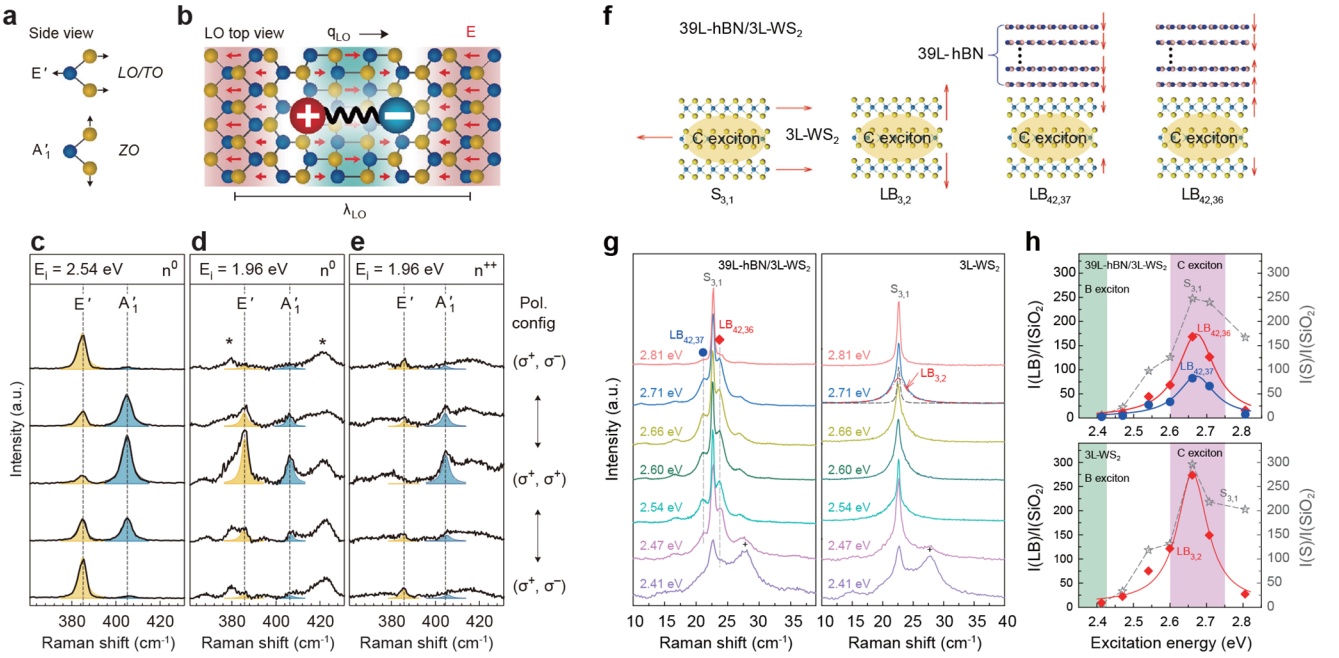

Figure 7. (a) Vibration patterns of the polar E' mode and homopolar A_1' mode of MoS_2. (b) Schematic of Fröhlich interaction between electrons (or excitons) and a macroscopic electric field induced by LO phonons. (c–e) Circularly polarized Raman spectra of 1L-MoS_2 under (c) nonresonant excitation and low charge carrier density, (d) resonant excitation and low charge carrier density, and (e) resonant excitation and high charge carrier density. Reprinted by permission from Macmillan Publishers Ltd.: Miller, B.; Lindlau, J.; Bommert, M.; Neumann, A.; Yamaguchi, H.; Holleitner, A.; Högele, A.; Wurstbauer, U, *Nat. Commun.* **2019**, *10*, 807 (ref 112). Copyright 2019. (f) The normal mode displacements of the $S_{3,1}$, $LB_{3,2}$ in a standalone 3LW flake and $LB_{42,36}$, $LB_{42,37}$ modes in a 39L-hBN/3L-WS_2. (g) Raman spectra of 39L-hBN/3L-WS_2 and 3L-WS_2 with excitation energies in the range of 2.41–2.81 eV. (h) Resonant profiles of the $LB_{42,36}$, $LB_{42,37}$, and $S_{3,1}$ modes in 39L-hBN/3L-WS_2, and the $S_{3,1}$, $LB_{3,2}$ modes in 3L-WS_2. Reprinted by permission from Macmillan Publishers Ltd.: Lin, M.; Zhou, Y.; Wu, J.; Cong, X.; Liu, X.; Zhang, J.; Li, H.; Yao, W.; Tan, P. *Nat. Commun.* **2019**, *10*, 2419 (ref 93). Copyright 2019.

directly considers the interaction between rigid atomic layers[32,34,92] and the vdW model that considers the coupling of inter- and intralayer vibrations.[33,35] The force constant model used multiple force constants to represent the interaction between different rigid atomic layers, and the frequencies of the intra- and interlayer modes can be reproduced by solving the corresponding dynamic equations. However, this model cannot directly predict the frequency splitting between Davydov components from the measured frequencies of the intralayer modes of the monolayer 2DMs and interlayer modes of the corresponding bilayer 2DMs. In contrast, these frequencies can be predicted by the vdW model.[33] In *N*L-$MoTe_2$, the frequency difference between the *j*th Davydov component of the A_{1g}-like mode (ω_{cj}) and the frequency of the A_{1g} mode of the monolayer (ω_0) can be calculated by the relationship $\omega_{cj}^2 = \Delta\omega_j^2 + \omega_0^2$, where $\Delta\omega_j$ is the frequency of $LB_{N,j}$ mode.[33] Recently, Leng et al. observed all Davydov entities of A_1' and A_2'' modes in twisted multilayer $MoTe_2$ at 4 K.[35] The frequencies of the corresponding Davydov components can likewise be explained by the vdW model. However, due to the negligible interfacial shear coupling, the spectral profile of the Davydov components of the in-plane intralayer E' modes can be fitted by those of the corresponding E' modes of its constituents (Figure 6b).

Exciton–Phonon Interaction. The interactions between (quasi)particles (electrons, excitons, phonons, magnons, etc.) in 2DMs are fundamentally responsible for unusual quantum behavior. Understanding the interactions between (quasi)-particles is a prerequisite for achieving manipulation of relevant properties. Among these interactions, electron–phonon coupling is important for optical and electronic properties. For example, scattering of electrons by optical phonons dominates the mobility of 2DMs at room temperature;[107] electron–phonon or exciton–phonon interactions are important for rapid cooling of photoexcited carriers[108,109] and coherence of exciton luminescence.[110,111] As electron–phonon interactions are one fundamental process in Raman scattering, electron–phonon coupling directly dominates intensity, line shape, and polarization response of Raman modes. Studying Raman spectra of 2DMs in a wide excitation energy range has been widely used to study electron–phonon coupling in 2DMs, where photon–electron and electron–phonon interactions under different energy excitations should be involved. Particularly, the strength of the exciton–phonon interaction can be obtained by resonance Raman spectroscopy in semiconductors with strong excitonic effects, in which the real intermediate exciton-related states are involved in Raman scattering.

The enhanced Raman intensity of Raman modes in two-dimensional semiconductors in resonance Raman scattering is dependent on the symmetry of both the excitonic states and phonon modes involved in exciton–phonon coupling.[113−115] In isotropic 2DMs like MoS_2, the A and B excitons are dominated by the out-of-plane Mo-d_z^2 orbital and can couple to the out-of-plane A_{1g} phonon, while the C exciton is dominated by both the out-of-plane Mo-d_z^2 orbital and in-plane S-p_x, p_y orbitals, making it well coupled to the in-plane E_{2g}^1 phonons.[113,116] Therefore, the A_{1g} mode is significantly

https://doi.org/10.1021/acs.analchem.3c00272
Anal. Chem. 2023, 95, 10821−10838

enhanced at A and B exciton resonance, while the E^1_{2g} mode is significantly enhanced at C exciton resonance.[113,116] In contrast, in anisotropic 2DMs such as BP and ReS_2, both phonons and excitons may exhibit anisotropic properties, leading to more distinct effects on the corresponding Raman spectra due to symmetry-dependent exciton−phonon coupling.[55,117,118] For example, in few-layer BP, the bright exciton has a spatial distribution along the armchair direction, and the A^2_g mode in BP with atoms vibrating along the armchair direction exhibits stronger Raman intensity than the A^1_g mode with atoms vibrating along the out-of-plane direction.[115]

The exciton−phonon interaction in polar semiconductors can lead to the breakdown of the selection rules of specific Raman modes.[119−121] Generally, the electron−phonon interaction dominates the Raman tensors and further gives the polarization response of a certain Raman mode. In most cases of Raman scattering, two types of electron−phonon interactions are commonly considered.[29] The first type is the deformation potential interaction, which describes the alternations in the electronic energies induced by microscopic distortions within the unit cells. The second type is the Fröhlich interaction, which originates from the interaction between the electrons and the macroscopic longitudinal electric field produced by longitudinal optical (LO) phonons.[29] The contribution of the two types of interactions to the Raman tensor can vary with the excitation energies.[122] In the case of the polar semiconductor CdS, it has been demonstrated that under exciton resonance, the Fröhlich interaction between excitons and LO phonons becomes wavevector-dependent. Consequently, this leads to the significant change in corresponding Raman tensor and deviates from the selection rules.[29,119] For two-dimensional semiconductors, a similar phenomenon has also been observed. Drapcho et al. reported the breakdown of the Raman selection rule for the E' mode of 1L-MoS_2 at the A exciton resonance.[120] Compared to the case under nonresonant excitation, the E' mode appeared to redshift by around 3 cm^{-1} under resonant excitation, which was attributed to defect-assisted scattering of the phonon slightly away from the Γ point of the Brillouin zone. Miller et al. demonstrated that the E' mode is a polar mode and the Fröhlich interaction should be taken into account for exciton−phonon interaction in 1L-MoS_2 under A exciton resonance (Figure 7a,b).[112] The Raman tensor of Fröhlich interaction is significantly different from that of electron−phonon interaction based on deformation potential, and in most cases only the latter is considered in the Raman selection rule. Furthermore, they claimed that the Fröhlich interaction for the E' mode in 1L-MoS_2 is an impurity-assisted second-order Fröhlich exciton−LO phonon scattering process. The relative proportion of these two types of interactions varies with excitation energy, and the proportion of Fröhlich interaction increases significantly at A exciton resonance, which leads to anomalous polarization response of the E' mode (Figure 7c−e). Such exciton−LO phonon interaction can be suppressed by electron doping, which correlates with a distinct increase of the degree of valley polarization. The effects of temperature, dielectric screening, and other factors on Fröhlich interaction in MoS_2 were further investigated in detail.[123] Similar results and explanations have also been reported in WS_2.[121,124]

Peculiar exciton−phonon interactions also exist in vdWHs due to the interfacial coupling at the heterointerfaces. Excitons and phonons respectively in different constituents can interact with each other across the heterointerfaces, i.e., the interlayer exciton−phonon coupling, which was first observed in hBN/WSe_2 vdWHs.[125,126] The optically silent out-of-plane ZO phonon emerged in Raman spectra with strong intensities through resonant coupling to the A exciton of WSe_2 and a new hybrid state of vdWHs. In addition to the intralayer phonons, the interlayer phonons are more likely to interact with the exciton within each constituent of vdWHs. Lin et al. revealed the cross-dimensional electron−phonon coupling between LB phonons in WS_2/hBN vdWHs and excitonic states in WS_2 constitute.[93] Rich interlayer LB modes in WS_2/hBN vdWHs composed of tens to hundreds of hBN layers were observed, and the calculated energy band of vdWHs also indicated that the excitonic states are localized in the WS_2 constituent (Figure 7f). Through the analysis of the resonant profile of LB modes, they claimed that the strong interfacial coupling between hBN and WS_2 leads to the cross-dimensional coupling between the extended LB phonons and localized C excitons in WS_2 (Figure 7g,h). Two methods respectively based on the phonon wave function projection and interlayer bond polarizability were further proposed to reproduce the relative intensity of these LB modes, which also verified the physical origin of this special exciton−phonon interaction.[93] A similar mechanism also occurs in hBN/$MoTe_2$ vdWHs[94] and even in ternary vdWHs composed of hBN, graphene, and TMDs.[95]

Strain Effects. 2DMs exhibit ultrahigh stretchability and can experience strain when placed on nonuniform substrates or combined with other materials to form heterogeneous structures. This lattice compression and stretching alters the atom distance and causes a redistribution of electrons, ultimately impacting the electronic and optical properties of 2DMs.[129] The strain-induced changes in the phonon dispersion and electronic structure of 2DMs lead to variations of the frequency and intensity of Raman modes. Therefore, characterizing 2DMs under strain using Raman spectroscopy can provide access to the mechanical parameters of 2DMs and can help to understand the strain effect on their vibrational and electronic properties for both fundamental research and related device applications, particularly in the development of flexible wearable devices.

The application of strain to 2DMs results in changes to their chemical bond strength and structure, causing a shift in the frequency of the Raman mode. As with conventional solids, tensile strain in 2DMs enlarges the atomic distance and further enlarges the phonon softening, whereas compressive strain results in the phonon stiffening. Moreover, the phonon modes exhibiting higher sensitivity to strain typically have the atom vibration direction aligned with the strain direction. In-plane degenerate modes generally split under uniaxial strain due to lattice distortion and reduction in symmetry. The above conclusions can apply to most in-plane isotropic 2DMs under uniaxial strain, such as the G mode in graphene[130,131] and the E^1_{2g}/A_{1g} modes in MoS_2.[132,133] For in-plane anisotropic materials, such as BP, the frequency shift of the characteristic Raman modes under uniaxial strain also depends on the strain direction.[134,135] In addition, the interlayer vibration modes of multilayer 2DMs show anomalous behavior under uniaxial strain, which arises from the inevitable coupling between interlayer shear and in-plane uniaxial strain.[136] Splitting of the interlayer shear mode of bilayer MoS_2 has been reported under tensile strain, and the split shear mode is hardened rather than softened along the strain direction, in contrast to the case of intralayer A_{1g} phonons. Generally, the mechanical constants such as Grüneisen parameter, shear deformation potential, and

https://doi.org/10.1021/acs.analchem.3c00272
Anal. Chem. 2023, 95, 10821−10838

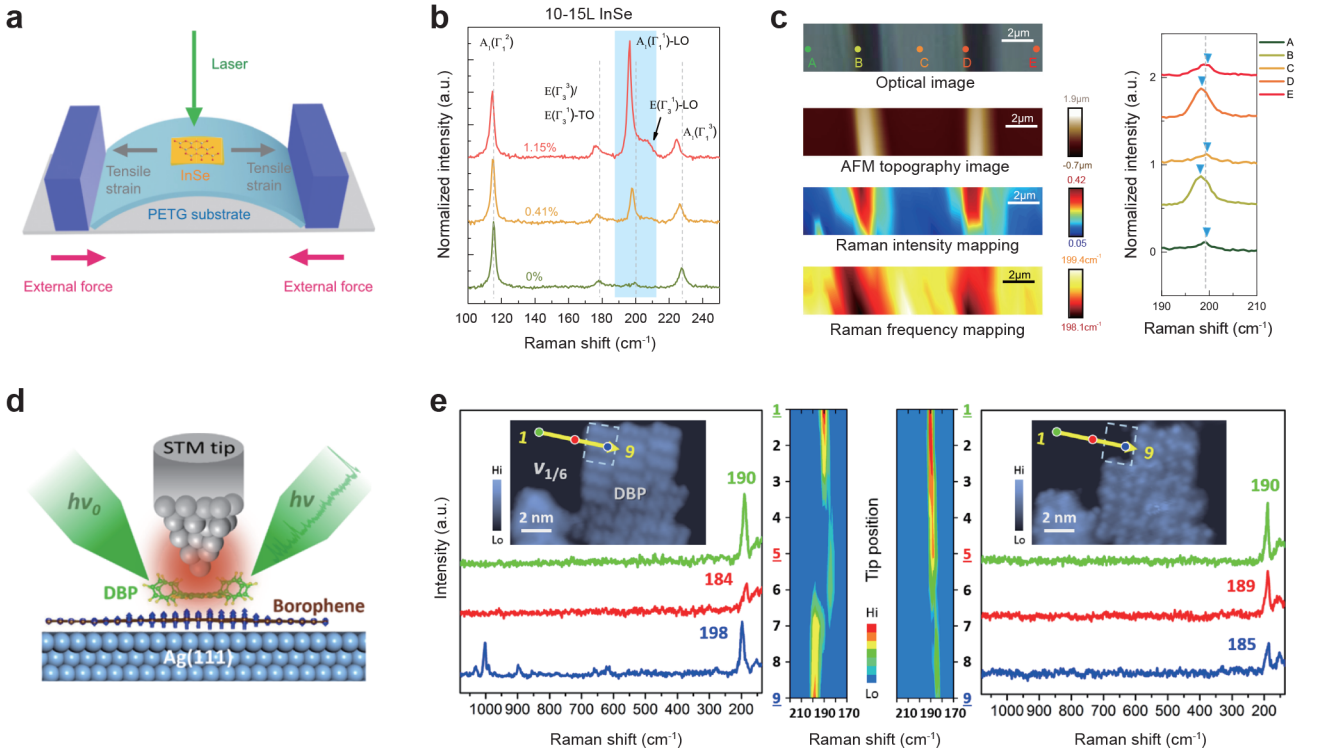

Figure 8. (a) Experimental schematic of resonance Raman experiments on few-layer InSe exfoliated on flexible poly(ethylene terephthalate)-glycol (PETG) substrates under tensile strain. (b) Raman spectra of 10−15L InSe under the excitation energy of 2.41 eV as uniaxial tensile strain is applied from 0% to 1.15%. (c) Left panel: optical image, AFM topography image, intensity mapping, and frequency mapping of $A_1(\Gamma_1^1)$-LO mode of wrinkled InSe. The colored points correspond to different flat and wrinkled areas. Right panel: Raman spectra of the $A_1(\Gamma_1^1)$-LO mode were recorded at the five points indicated in the optical image. Reproduced from Song, C.; Fan, F.; Xuan, N.; Huang, S.; Wang, C.; Zhang, G.; Wang, F.; Xing, Q.; Lei, Y.; Sun, Z.; Wu, H.; Yan, H. *Phys. Rev. B* **2019**, *99*, 195414 (ref 127). Copyright 2019 American Physical Society. (d) Experimental schematic of STM-TERS experiments on DBP/borophene heterostructure. (e) TERS spectra of DBP/borophene heterostructure acquired before (left) and after (right) removal of two DBP molecules at color-marked sites in the inset STM image. The frequencies of the B_{3g}^2 mode are marked out. Spectral evolution of the B_{3g}^2 mode along the yellow-line trace is also depicted (middle panel). Reproduced from Li, L.; Schultz, J.; Mahapatra, S.; Liu, X.; Shaw, C.; Zhang, X.; Hersam, M.; Jiang, N. *J. Am. Chem. Soc.* **2021**, *143* (38), 15624−15634 (ref 128). Copyright 2021 American Chemical Society.

Poisson's ratio of 2DMs can be determined by analyzing the frequency shift of the Raman modes as a function of the strain magnitude.[129]

The strain-induced alteration of the electronic structure in 2DMs impacts the photon−electron and electron−phonon interactions, which can be revealed from the Raman intensity. For instance, Song et al. performed resonance Raman spectroscopy to study the vibrational and electronic properties of few-layer InSe under uniaxial tensile strain with a two-point bending apparatus (Figure 8a).[127] They found that the applied tensile strain caused significant enhancement of two LO modes under an excitation energy of 2.41 eV (Figure 8b). This enhancement effect was attributed to the modulation of the electronic structure of InSe by tensile strain. Analysis of the energy change of excitonic states under strain showed that the tensile strain causes a redshift of the B exciton energy of few-layer InSe, which is perfectly matched with the excitation energy, thereby enhancing the two specific LO modes.

On the basis of the understanding of the strain effect on the frequency and intensity of Raman modes, Raman characterization of specific modes in 2DMs can be used to gather information on the magnitude and spatial distribution of strain. With the high sensitivity of the LO mode intensity to strain, Raman intensity mapping of the LO mode of the wrinkled few-layer InSe under the excitation energy of 2.41 eV shows a clear spatial distribution of strain, which is highly consistent with the morphology image obtained by AFM (Figure 8c).[127] Besides the homogeneous strain applied by mechanical devices, localized strain typically exists in nanostructures, and it can be characterized using TERS. Recently, Li et al. realized the vertical integration of borophene with tetraphenyldibenzoperiflanthene (DBP) and employed UHV-TERS to perform angstrom-scale characterization of the subtle ripples and compressive strains of the borophene lattice underneath the molecular layer (Figure 8d).[128] The magnitude of the interfacial strain was determined to be ∼0.6% and highly concentrated in the range of 1−1.5 nm near the edge of the heterostructure by comparing the results of line mapping before and after the removal of organic molecules with the calculated frequency shift of the B_{3g}^2 mode under biaxial strain (Figure 8e).

Doping Effects. Doping is an effective method to modulate the electronic structure and phase transition of 2DMs. The primary implementations of doping include electrostatic doping, substitution doping, and surface charge transfer doping.[137−140] Additional electrons or holes introduced by doping can significantly alter the carrier concentration and Fermi level (E_F) of 2DMs, leading to potential applications in electronic/optoelectronic devices and chemical reactions. Doping can directly influence the photon−electron

https://doi.org/10.1021/acs.analchem.3c00272
Anal. Chem. 2023, 95, 10821−10838

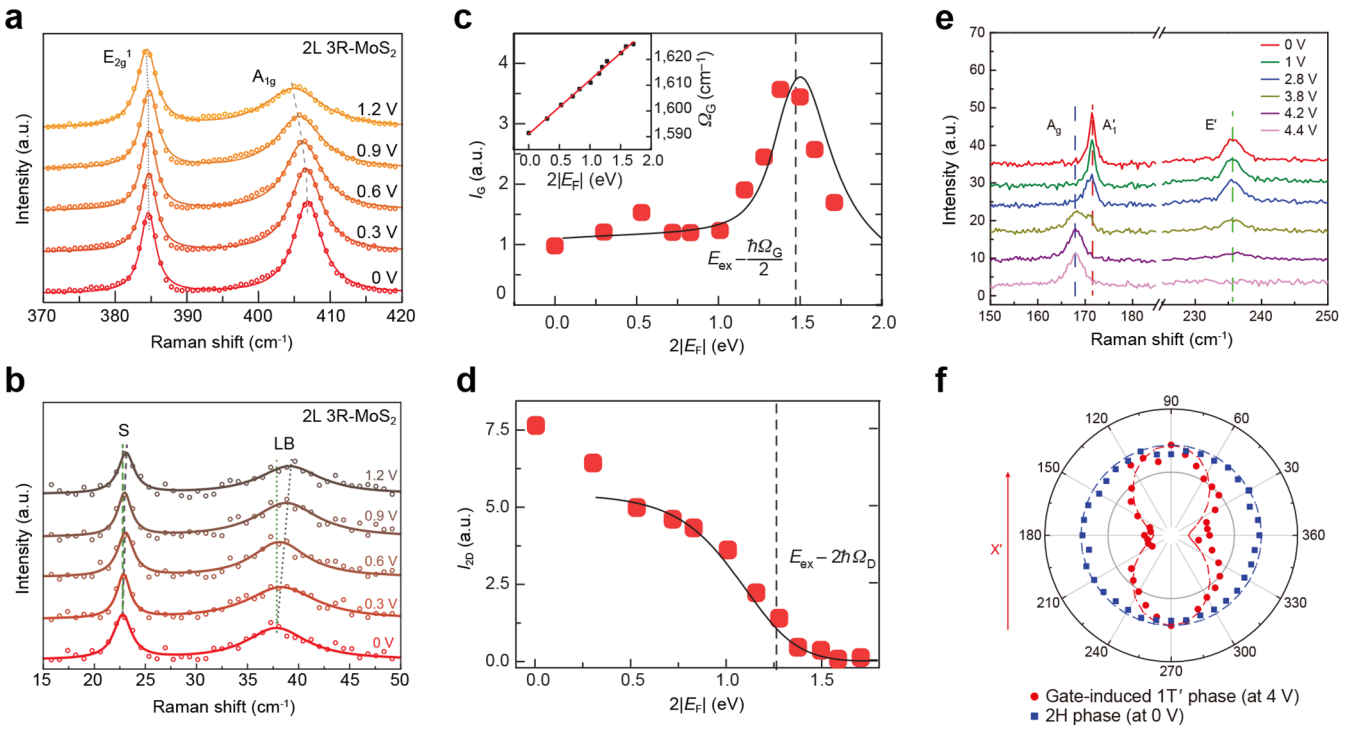

Figure 9. (a) High-frequency and (b) low-frequency Raman spectra of bilayer 3R-MoS_2 at different gate voltages under the excitation energy of 2.33 eV. Reproduced from Zhang, X.; Zhu, T.; Huang, J.; Wang, Q.; Cong, X.; Bi, X.; Tang, M.; Zhang, C.; Zhou, L.; Zhang, D.; Su, T.; Dai, X.; Meng, K.; Li, Z.; Qiu, C.; Zhao, W.; Tan, P.; Zhang, H.; Yuan, H. *ACS Appl. Mater. Interfaces* **2020**, *12*, 46900−46907 (ref 141). Copyright 2020 American Chemical Society. (c) Raman intensity of the G mode as a function of $2|E_F|$ (symbols). Black line: theoretical prediction. Inset: doping dependence of the G mode frequency. Ω_G: the frequency of the G mode. (d) Doping dependence of the 2D mode Raman intensity (symbols). Black line: prediction by two-phonon Raman scattering theory. Ω_{2D}: frequency of the 2D mode. Reprinted by permission from Macmillan Publishers Ltd.: Chen, C.; Park, C.; Boudouris, B.; Horng, J.; Geng, B.; Girit, C.; Zettl, A.; Crommie, M.; Segalman, R.; Louie, S.; Wang, F., *Nature* **2011**, *471*, 617−620 (ref 138). Copyright 2011. (e) Raman evolution upon the phase transition from 2H to 1T′ phase, as the bias changes from 0 to 4.4 V. A_1' and E' modes are the characteristic Raman modes of the 2H phase, while the A_g mode is the characteristic mode of the 1T′ phase. (f) Polarized Raman spectra of $MoTe_2$ in the pristine 2H phase and in the gate-induced 1T′ phase. Reprinted by permission from Macmillan Publishers Ltd.: Wang, Y.; Xiao, J.; Zhu, H.; Li, Y.; Alsaid, Y.; Fong, K.; Zhou, Y.; Wang, Y.; Zettl, A.; Reed, E.; Zhang, X., *Nature* **2017**, *550*, 487−491 (ref 139). Copyright 2017.

and electron−phonon interactions in Raman scattering, which are fully reflected in the spectral features of the Raman modes. Moreover, the doping-induced phase transition of 2DMs may directly change crystal structures, which can be captured from the change in Raman modes. Therefore, Raman spectroscopy can provide rich information about the doping-induced properties of 2DMs.

Different types and concentrations of doping can change the lattice constants of 2DMs and affect the electron−phonon interaction in Raman processes, which results in the drastic change in the frequency and line width of Raman modes.[142−144] However, it should be noted that not all Raman modes of certain 2DMs are sensitive to charge doping, and symmetry plays a crucial role in determining whether a mode is doping-sensitive. In the case of electron (hole) doping of MoS_2 and BP, the occupation of the bottom (top) of the conduction (valence) band states is expected, and if their symmetry representations are orthogonal to that of phonon, the corresponding electron−phonon coupling matrix element will be null, leading to insensitivity to doping.[145,146] Therefore, the E^1_{2g} mode in 1L-MoS_2 exhibits insensitivity to electron doping compared with A_{1g} for weak coupling to the electronic states at K point (conduction band minimum) with A_{1g} symmetry.[145,147] It is also the case for the doping sensitivity of A^1_g, A^2_g, and B_{2g} modes in BP flakes.[146]

Doping-sensitive Raman modes in several typical 2DMs such as TMDs and BP exhibit red shift and broaden line width upon electron doping.[145,146,148,149] An exception is the G mode of graphene, which exhibits a blue shift and reduced line width after doping.[142,150] The strong electron−phonon coupling between electrons at K valley and E_{2g} phonon of the G mode leads to a Kohn anomaly that decreases the G mode frequency in pristine graphene.[151] However, such strong coupling is suppressed after doping, resulting in a blue shift and reduced line width of the G mode in doped graphene.[142] Interestingly, the response of interlayer modes may exhibit different behavior from that of the intralayer modes since the frequencies of the interlayer modes are more sensitive to the interlayer distance and the charge density distribution of each layer. For instance, the frequency of the S mode of multilayer graphene with hole doping decreases significantly with increasing hole concentration, which is attributed to the decreased interlayer distance.[140] Recently, a study of electrostatic doping effects in bilayer 3R-MoS_2 by Zhang et al. revealed an increase in the S and LB mode frequencies, which is in contrast with that in intralayer A_{1g} mode and indicates a decrease in layer spacing with enhanced interlayer coupling (Figure 9a,b).[141]

Doping directly affects the optical transition process by altering the occupied state of electrons in the energy band of the crystal, which inevitably affects the intensity of Raman

https://doi.org/10.1021/acs.analchem.3c00272
Anal. Chem. 2023, 95, 10821−10838

modes in 2DMs. This point needs to be understood in terms of the microscopic processes of Raman scattering. Figure 1 has elucidated the first- and second-order Raman scattering processes, where the choice of initial and intermediate states can be arbitrary, provided that energy and momentum conservation are satisfied. This will lead to many scattering processes involving different electronic states, which are referred to as different scattering pathways. For a specific Raman mode, its intensity should contain the contributions from all scattering pathways. Electron doping will result in the occupation of the previously unoccupied electronic states, while the opposite is true for hole doping. Therefore, doping will reduce the number of scattering pathways of the Raman mode, thus affecting its intensity.[138,152] The study of the variation of the G mode intensity of graphene with doping concentration reveals that there is a significant quantum interference between the scattering pathways of the G mode.[138] When some of the scattering pathways are blocked due to doping, the G mode intensity does not diminish as usually expected but instead is dramatically enhanced (Figure 9c). In contrast, for the 2D mode originating from triple resonance Raman scattering, there is no quantum interference phenomenon between the scattering pathways. When all the resonance pathways are blocked, the 2D mode intensity becomes zero (Figure 9d).[138] The 2D mode can be observed when the excitation energy (E_{ex}) and the energy of the 2D mode (E_{2D}) satisfy $(E_{ex} - E_{2D})/2 > E_F$, which also provides a means to determine the E_F of doped graphene.[137]

In addition to the modulation of the electronic properties, doping may also induce structural phase transitions in 2DMs, which can significantly affect the Raman modes. As a result, Raman spectroscopy has become an important tool for monitoring the phase transitions of 2DMs based on doping. As a typical multiphase material, TMDs can be in 2H (thermodynamically stable, semiconductor phase), 1T (substable, metallic phase), and 1T′ (distorted 1T phase) stacking phases.[5] Doping can drive the interconversion between different phases by changing the electron filling of the *d* orbital of transition metal atoms. The transition of 2H to 1T′ phase of $MoTe_2$ was first observed by Wang et al. through electrostatic doping (Figure 9e).[139] The intensity ratio of Raman modes between different phases exhibits hysteresis under electric field scanning: $F = 1T'(A_g)/(2H(A_1') + 1T'(A_g))$. Moreover, the polarized Raman spectra indicate the transition from the in-plane isotropy of the 2H phase to the anisotropy of the 1T′ phase (Figure 9f). Further studies have revealed that such phase transition can also occur in thick $MoTe_2$, while more layers will result in higher voltages to induce phase transition.[153] Dhakal et al. observed different phases of bulk MoS_2 by Raman scattering that range from heavily doped 2H phase to a distorted lattice phase and then on to a complete 1T′ phase using $MoS_2/[Ca_2N]^+ \cdot e^-$ heterostructures, in which kinetic free electrons were directly injected into MoS_2.[154]

SUMMARY AND OUTLOOK

This review focuses on characterizing the fundamental properties of 2DMs and vdWHs with different Raman techniques. The characterization involves various aspects, including crystalline anisotropy, structural defects, interlayer coupling, exciton−phonon interaction, strain effects, and doping effects at different spatial scales. Standard micro-Raman spectroscopy provides a quick and effective method for characterizing defects, doping concentrations, and strain magnitudes in 2DMs. Advances in polarized Raman spectroscopy, low-frequency Raman spectroscopy, and resonance Raman spectroscopy offer valuable insights into the crystalline anisotropy, interlayer coupling, and exciton−phonon interactions of both 2DMs and vdWHs. Moreover, the enhancement of Raman signal by TERS allows the detection of weak local signals, and the spatial resolution beyond the limit of optical diffraction can be directly used to analyze the surface and local features of 2DMs at the nanoscale.

Raman studies on 2DMs predominantly rely on micro-Raman spectroscopy, which cannot provide property information at the nanoscale due to its limited spatial resolution. However, TERS shows its potential to overcome this limitation, which has been demonstrated in studying the nanoscale properties of certain 2DMs. Currently, TERS is constrained in its applicability to a limited range of 2DM types. Thus, future advances in TERS should aim to achieve nanoscale characterization of more types of 2DMs. Future Raman research should also prioritize exploring the physical properties of newly discovered 2DMs and novel nanostructures. Among the most prominent 2DMs, magnetic 2DMs exhibit distinctive properties due to their additional magnetic freedom. The complex interactions among quasi-particles in magnetic 2DMs give rise to unique features in Raman spectra.[155−158] Additionally, vdWHs composed of different types of 2DMs through artificial stacking offer exciting prospects for Raman studies, as they exhibit exceptional properties distinct from those of their constituent materials due to interfacial coupling. The interfacial twist angle also introduces new possibilities for manipulating the properties of 2DMs. Smaller twist angles can induce lattice reconstructions[103] and the formation of moiré superlattices, resulting in phonon localization.[159] Investigation of this phenomenon aligns precisely with the research interests of TERS.

AUTHOR INFORMATION

Corresponding Author

Ping-Heng Tan − *State Key Laboratory of Superlattices and Microstructures, Institute of Semiconductors, Chinese Academy of Sciences, Beijing 100083, China; Center of Materials Science and Optoelectronics Engineering & CAS Center of Excellence in Topological Quantum Computation, University of Chinese Academy of Sciences, Beijing 100049, China;* orcid.org/0000-0001-6575-1516; Email: phtan@semi.ac.cn

Authors

Heng Wu − *State Key Laboratory of Superlattices and Microstructures, Institute of Semiconductors, Chinese Academy of Sciences, Beijing 100083, China; Center of Materials Science and Optoelectronics Engineering & CAS Center of Excellence in Topological Quantum Computation, University of Chinese Academy of Sciences, Beijing 100049, China*

Miao-Ling Lin − *State Key Laboratory of Superlattices and Microstructures, Institute of Semiconductors, Chinese Academy of Sciences, Beijing 100083, China;* orcid.org/0000-0001-5838-8237

Yan Zhou − *State Key Laboratory of Superlattices and Microstructures, Institute of Semiconductors, Chinese Academy of Sciences, Beijing 100083, China*

https://doi.org/10.1021/acs.analchem.3c00272
Anal. Chem. 2023, 95, 10821−10838

Xin Zhang − *State Key Laboratory of Superlattices and Microstructures, Institute of Semiconductors, Chinese Academy of Sciences, Beijing 100083, China;* orcid.org/0000-0002-1450-2525

Complete contact information is available at: https://pubs.acs.org/10.1021/acs.analchem.3c00272

Notes

The authors declare no competing financial interest.

Biographies

Heng Wu is currently a Ph.D. candidate under the supervision of Prof. Ping-Heng Tan at Institute of Semiconductors, Chinese Academy of Sciences. He received his B.S. degree from Huazhong University of Science and Technology in 2020. His research is primarily on the optical properties of two-dimensional semiconductors and heterostructures.

Miao-Ling Lin is now an associate professor in the State Key Laboratory of Superlattices and Microstructures at the Institute of Semiconductors, Chinese Academy of Sciences. She obtained her Ph.D. degree from the Institute of Semiconductors, Chinese Academy of Sciences in 2019. She received her B.S. degree from Nankai University in 2014. Her current research interest focuses on optical properties of quantum materials, low-dimensional semiconductor materials, and related heterostructures.

Yan Zhou is now a postdoc and research associate at Institute of Semiconductors, Chinese Academy of Sciences and University of Bristol. He obtained his Ph.D. degree in Physics from University of Bristol (2018) and M.S degree from Northwestern Polytechnical University (2014). His current research focuses on low-dimensional semiconductors based optical properties and micro-to-nanoscale thermal transport under extreme conditions.

Xin Zhang is a professor in the State Key Laboratory of Superlattices and Microstructures at the Institute of Semiconductors, Chinese Academy of Sciences. He obtained B.S. degree (2010) in Physics from Soochow University and Ph.D. degree (2015) from the Institute of Semiconductors, Chinese Academy of Sciences. He worked at Centre national de la recherche scientifique (France), Nanyang Technological University (Singapore), and Concordia University (Canada) as a Postdoc Research Associate from 2016-2020. His current research focuses on low-dimensional semiconductor nano-optical electromechanical system.

Ping-Heng Tan is a professor in the State Key Laboratory of Superlattices and Microstructures at the Institute of Semiconductors, Chinese Academy of Sciences. He obtained B.S. degree (1996) in Physics from Peking University and Ph.D. degree (2001) from the Institute of Semiconductors, Chinese Academy of Sciences. He worked at Walter Schottky Institut, Technische Universitaet Muenchen as a Postdoc Research Associate from 2001-2003. He was a KC-Wong Royal Society Fellow at Cambridge University from 2006-2007. His current research is on two-dimensional layered materials, nanocarbon materials, topological insulators and novel low-dimensional semiconductor optoelectronic materials. He was supported by the National Science Fund for Distinguished Young Scholars in 2012.

■ ACKNOWLEDGMENTS

The authors acknowledge support from National Natural Science Foundation of China (Grant Nos. 12004377, 11874350, and 12204472), CAS Key Research Program of Frontier Sciences (Grant Nos. ZDBS-LY-SLH004 and XDPB22), and CAS Project for Young Scientists in Basic Research (Grant No. YSBR-026).

■ REFERENCES

(1) Novoselov, K. S.; Geim, A. K.; Morozov, S. V.; Jiang, D.; Zhang, Y.; Dubonos, S. V.; Grigorieva, I. V.; Firsov, A. A. *Science* **2004**, *306*, 666−669.
(2) Mak, K. F.; Lee, C.; Hone, J.; Shan, J.; Heinz, T. F. *Phys. Rev. Lett.* **2010**, *105*, 136805.
(3) Splendiani, A.; Sun, L.; Zhang, Y.; Li, T.; Kim, J.; Chim, C.-Y.; Galli, G.; Wang, F. *Nano Lett.* **2010**, *10*, 1271−1275.
(4) Wang, Q. H.; Kalantar-Zadeh, K.; Kis, A.; Coleman, J. N.; Strano, M. S. *Nat. Nanotechnol.* **2012**, *7*, 699−712.
(5) Manzeli, S.; Ovchinnikov, D.; Pasquier, D.; Yazyev, O. V.; Kis, A. *Nat. Rev. Mater.* **2017**, *2*, 17033.
(6) Li, L.; Yu, Y.; Ye, G. J.; Ge, Q.; Ou, X.; Wu, H.; Feng, D.; Chen, X. H.; Zhang, Y. *Nat. Nanotechnol.* **2014**, *9*, 372−377.
(7) Liu, H.; Neal, A. T.; Zhu, Z.; Luo, Z.; Xu, X.; Tománek, D.; Ye, P. D. *ACS Nano* **2014**, *8*, 4033−4041.
(8) Qiao, J.; Kong, X.; Hu, Z.-X.; Yang, F.; Ji, W. *Nat. Commun.* **2014**, *5*, 4475.
(9) Coleman, J. N.; Lotya, M.; O'Neill, A.; Bergin, S. D.; King, P. J.; Khan, U.; Young, K.; Gaucher, A.; De, S.; Smith, R. J.; Shvets, I. V.; Arora, S. K.; Stanton, G.; Kim, H.-Y.; Lee, K.; Kim, G. T.; Duesberg, G. S.; Hallam, T.; Boland, J. J.; Wang, J. J.; et al. *Science* **2011**, *331*, 568−571.
(10) Xi, X.; Wang, Z.; Zhao, W.; Park, J.-H.; Law, K. T.; Berger, H.; Forró, L.; Shan, J.; Mak, K. F. *Nat. Phys.* **2016**, *12*, 139−143.
(11) Wang, Q.-Y.; Li, Z.; Zhang, W.-H.; Zhang, Z.-C.; Zhang, J.-S.; Li, W.; Ding, H.; Ou, Y.-B.; Deng, P.; Chang, K.; Wen, J.; Song, C.-L.; He, K.; Jia, J.-F.; Ji, S.-H.; Wang, Y.-Y.; Wang, L.-L.; Chen, X.; Ma, X.-C.; Xue, Q.-K. *Chin. Phys. Lett.* **2012**, *29*, No. 037402.
(12) Zhang, H.; Liu, C.-X.; Qi, X.-L.; Dai, X.; Fang, Z.; Zhang, S.-C. *Nat. Phys.* **2009**, *5*, 438−442.
(13) Gibertini, M.; Koperski, M.; Morpurgo, A. F.; Novoselov, K. S. *Nat. Nanotechnol.* **2019**, *14*, 408−419.
(14) Huang, B.; Clark, G.; Navarro-Moratalla, E.; Klein, D. R.; Cheng, R.; Seyler, K. L.; Zhong, D.; Schmidgall, E.; McGuire, M. A.; Cobden, D. H.; Yao, W.; Xiao, D.; Jarillo-Herrero, P.; Xu, X. *Nature* **2017**, *546*, 270−273.
(15) Tan, C.; Cao, X.; Wu, X.-J.; He, Q.; Yang, J.; Zhang, X.; Chen, J.; Zhao, W.; Han, S.; Nam, G.-H.; Sindoro, M.; Zhang, H. *Chem. Rev.* **2017**, *117*, 6225−6331.
(16) Ferrari, A. C.; Basko, D. M. *Nat. Nanotechnol.* **2013**, *8*, 235−246.
(17) Novoselov, K. S.; Mishchenko, A.; Carvalho, A.; Castro Neto, A. H. *Science* **2016**, *353*, aac9439.
(18) Liu, Y.; Weiss, N. O.; Duan, X.; Cheng, H.-C.; Huang, Y.; Duan, X. *Nat. Rev. Mater.* **2016**, *1*, 16042.
(19) Tan, P.-H., Ed. *Raman Spectroscopy of Two-Dimensional Materials*; Springer Series in Materials Science; Springer: Singapore, Vol. *276*.
(20) Kim, J.; Lee, J.-U.; Cheong, H. *J. Phys.: Condens. Matter* **2020**, *32*, 343001.
(21) Pimenta, M. A.; Resende, G. C.; Ribeiro, H. B.; Carvalho, B. R. *Phys. Chem. Chem. Phys.* **2021**, *23*, 27103−27123.
(22) Tan, P. H.; Han, W. P.; Zhao, W. J.; Wu, Z. H.; Chang, K.; Wang, H.; Wang, Y. F.; Bonini, N.; Marzari, N.; Pugno, N.; Savini, G.; Lombardo, A.; Ferrari, A. C. *Nat. Mater.* **2012**, *11*, 294−300.
(23) Zhang, X.; Han, W. P.; Wu, J. B.; Milana, S.; Lu, Y.; Li, Q. Q.; Ferrari, A. C.; Tan, P. H. *Phys. Rev. B* **2013**, *87*, 115413.
(24) Liang, L.; Zhang, J.; Sumpter, B. G.; Tan, Q.-H.; Tan, P.-H.; Meunier, V. *ACS Nano* **2017**, *11*, 11777−11802.
(25) Ding, S.-Y.; Yi, J.; Li, J.-F.; Ren, B.; Wu, D.-Y.; Panneerselvam, R.; Tian, Z.-Q. *Nat. Rev. Mater.* **2016**, *1*, 16021.
(26) Wang, X.; Huang, S.-C.; Hu, S.; Yan, S.; Ren, B. *Nat. Rev. Phys.* **2020**, *2*, 253−271.

(27) Zhang, R.; Zhang, Y.; Dong, Z. C.; Jiang, S.; Zhang, C.; Chen, L. G.; Zhang, L.; Liao, Y.; Aizpurua, J.; Luo, Y.; Yang, J. L.; Hou, J. G. *Nature* **2013**, *498*, 82−86.
(28) Cong, X.; Li, Q.-Q.; Zhang, X.; Lin, M.-L.; Wu, J.-B.; Liu, X.-L.; Venezuela, P.; Tan, P.-H. *Carbon* **2019**, *149*, 19−24.
(29) Yu, P. Y.; Cardona, M. *Fundamentals of Semiconductors*; Graduate Texts in Physics; Springer: Berlin, 2010.
(30) Loudon, R. *Adv. Phys.* **1964**, *13*, 423−482.
(31) Zhang, X.; Qiao, X.-F.; Shi, W.; Wu, J.-B.; Jiang, D.-S.; Tan, P.-H. *Chem. Soc. Rev.* **2015**, *44*, 2757−2785.
(32) Froehlicher, G.; Lorchat, E.; Fernique, F.; Joshi, C.; Molina-Sánchez, A.; Wirtz, L.; Berciaud, S. *Nano Lett.* **2015**, *15*, 6481−6489.
(33) Song, Q. J.; Tan, Q. H.; Zhang, X.; Wu, J. B.; Sheng, B. W.; Wan, Y.; Wang, X. Q.; Dai, L.; Tan, P. H. *Phys. Rev. B* **2016**, *93*, 115409.
(34) Kim, K.; Lee, J.-U.; Nam, D.; Cheong, H. *ACS Nano* **2016**, *10*, 8113−8120.
(35) Leng, Y.-C.; Lin, M.-L.; Zhou, Y.; Wu, J.-B.; Meng, D.; Cong, X.; Li, H.; Tan, P.-H. *Nanoscale* **2021**, *13*, 9732−9739.
(36) Ferrari, A. C.; Meyer, J. C.; Scardaci, V.; Casiraghi, C.; Lazzeri, M.; Mauri, F.; Piscanec, S.; Jiang, D.; Novoselov, K. S.; Roth, S.; Geim, A. K. *Phys. Rev. Lett.* **2006**, *97*, 187401.
(37) Stenger, I.; Schué, L.; Boukhicha, M.; Berini, B.; Plaçais, B.; Loiseau, A.; Barjon, J. *2D Mater.* **2017**, *4*, No. 031003.
(38) Zhao, Y.; Luo, X.; Li, H.; Zhang, J.; Araujo, P. T.; Gan, C. K.; Wu, J.; Zhang, H.; Quek, S. Y.; Dresselhaus, M. S.; Xiong, Q. *Nano Lett.* **2013**, *13*, 1007−1015.
(39) Mao, N.; Lin, Y.; Bie, Y.-Q.; Palacios, T.; Liang, L.; Saito, R.; Ling, X.; Kong, J.; Tisdale, W. A. *Nano Lett.* **2021**, *21*, 4809−4815.
(40) He, R.; Yan, J.-A.; Yin, Z.; Ye, Z.; Ye, G.; Cheng, J.; Li, J.; Lui, C. H. *Nano Lett.* **2016**, *16*, 1404−1409.
(41) Qiao, X.-F.; Wu, J.-B.; Zhou, L.; Qiao, J.; Shi, W.; Chen, T.; Zhang, X.; Zhang, J.; Ji, W.; Tan, P.-H. *Nanoscale* **2016**, *8*, 8324−8332.
(42) Wu, J.-B.; Hu, Z.-X.; Zhang, X.; Han, W.-P.; Lu, Y.; Shi, W.; Qiao, X.-F.; Ijiäs, M.; Milana, S.; Ji, W.; Ferrari, A. C.; Tan, P.-H. *ACS Nano* **2015**, *9*, 7440−7449.
(43) Liu, X.-L.; Zhang, X.; Lin, M.-L.; Tan, P.-H. *Chinese Phys. B* **2017**, *26*, No. 067802.
(44) Chen, S.-Y.; Zheng, C.; Fuhrer, M. S.; Yan, J. *Nano Lett.* **2015**, *15*, 2526−2532.
(45) Tan, P. H.; Bougeard, D.; Abstreiter, G.; Brunner, K. *Appl. Phys. Lett.* **2004**, *84*, 2632−2634.
(46) Boukhicha, M.; Calandra, M.; Measson, M.-A.; Lancry, O.; Shukla, A. *Phys. Rev. B* **2013**, *87*, 195316.
(47) Verma, P. *Chem. Rev.* **2017**, *117*, 6447−6466.
(48) Sheng, S.; Wu, J.-b.; Cong, X.; Li, W.; Gou, J.; Zhong, Q.; Cheng, P.; Tan, P.-h.; Chen, L.; Wu, K. *Phys. Rev. Lett.* **2017**, *119*, 196803.
(49) Sheng, S.; Wu, J.-B.; Cong, X.; Zhong, Q.; Li, W.; Hu, W.; Gou, J.; Cheng, P.; Tan, P.-H.; Chen, L.; Wu, K. *ACS Nano* **2019**, *13*, 4133−4139.
(50) Huang, T.-X.; Cong, X.; Wu, S.-S.; Lin, K.-Q.; Yao, X.; He, Y.-H.; Wu, J.-B.; Bao, Y.-F.; Huang, S.-C.; Wang, X.; Tan, P.-H.; Ren, B. *Nat. Commun.* **2019**, *10*, 5544.
(51) Zhang, X.; Tan, Q.-H.; Wu, J.-B.; Shi, W.; Tan, P.-H. *Nanoscale* **2016**, *8*, 6435−6450.
(52) Wu, J.; Mao, N.; Xie, L.; Xu, H.; Zhang, J. *Angew. Chem., Int. Ed.* **2015**, *54*, 2366−2369.
(53) Kim, M.; Han, S.; Kim, J. H.; Lee, J.-U.; Lee, Z.; Cheong, H. *2D Mater.* **2016**, *3*, No. 034004.
(54) Huang, S.; Tatsumi, Y.; Ling, X.; Guo, H.; Wang, Z.; Watson, G.; Puretzky, A. A.; Geohegan, D. B.; Kong, J.; Li, J.; Yang, T.; Saito, R.; Dresselhaus, M. S. *ACS Nano* **2016**, *10*, 8964−8972.
(55) Wang, X.; Jones, A. M.; Seyler, K. L.; Tran, V.; Jia, Y.; Zhao, H.; Wang, H.; Yang, L.; Xu, X.; Xia, F. *Nat. Nanotechnol.* **2015**, *10*, 517−521.
(56) Luo, Z.; Maassen, J.; Deng, Y.; Du, Y.; Garrelts, R. P.; Lundstrom, M. S.; Ye, P. D.; Xu, X. *Nat. Commun.* **2015**, *6*, 8572.
(57) Wang, H.; Chen, M.-L.; Zhu, M.; Wang, Y.; Dong, B.; Sun, X.; Zhang, X.; Cao, S.; Li, X.; Huang, J.; Zhang, L.; Liu, W.; Sun, D.; Ye, Y.; Song, K.; Wang, J.; Han, Y.; Yang, T.; Guo, H.; Qin, C.; et al. *Nat. Commun.* **2019**, *10*, 2302.
(58) Zhou, Z.; Cui, Y.; Tan, P.-H.; Liu, X.; Wei, Z. *J. Semicond.* **2019**, *40*, No. 061001.
(59) Zhang, J.; Zhou, Y.; Ying, P.; Sun, H.; Zhou, J.; Wang, T.; Jie, W.; Kuball, M. *Nanotechnology* **2020**, *31*, 165706.
(60) Zhou, Y.; Zhou, S.; Ying, P.; Zhao, Q.; Xie, Y.; Gong, M.; Jiang, P.; Cai, H.; Chen, B.; Tongay, S.; Zhang, J.; Jie, W.; Wang, T.; Tan, P.; Liu, D.; Kuball, M. *J. Phys. Chem. Lett.* **2022**, *13*, 3831−3839.
(61) Ribeiro, H. B.; Pimenta, M. A.; de Matos, C. J. S.; Moreira, R. L.; Rodin, A. S.; Zapata, J. D.; de Souza, E. A. T.; Castro Neto, A. H. *ACS Nano* **2015**, *9*, 4270−4276.
(62) Kim, J.; Lee, J.-U.; Lee, J.; Park, H. J.; Lee, Z.; Lee, C.; Cheong, H. *Nanoscale* **2015**, *7*, 18708−18715.
(63) Lin, M.-L.; Leng, Y.-C.; Cong, X.; Meng, D.; Wang, J.; Li, X.-L.; Yu, B.; Liu, X.-L.; Yu, X.-F.; Tan, P.-H. *Science Bulletin* **2020**, *65*, 1894−1900.
(64) Zou, B.; Wei, Y.; Zhou, Y.; Ke, D.; Zhang, X.; Zhang, M.; Yip, C.-T.; Chen, X.; Li, W.; Sun, H. *Nanoscale Horiz.* **2021**, *6*, 809−818.
(65) Choi, Y.; Kim, K.; Lim, S. Y.; Kim, J.; Park, J. M.; Kim, J. H.; Lee, Z.; Cheong, H. *Nanoscale Horiz.* **2020**, *5*, 308−315.
(66) Wang, J.; Luo, X.; Li, S.; Verzhbitskiy, I.; Zhao, W.; Wang, S.; Quek, S. Y.; Eda, G. *Adv. Funct. Mater.* **2017**, *27*, 1604799.
(67) Lee, C.; Jeong, B. G.; Yun, S. J.; Lee, Y. H.; Lee, S. M.; Jeong, M. S. *ACS Nano* **2018**, *12*, 9982−9990.
(68) Rhodes, D.; Chae, S. H.; Ribeiro-Palau, R.; Hone, J. *Nat. Mater.* **2019**, *18*, 541−549.
(69) Sun, T.; Zhang, G.; Xu, D.; Lian, X.; Li, H.; Chen, W.; Su, C. *Mater. Today Energy* **2019**, *12*, 215−238.
(70) Liang, Q.; Zhang, Q.; Zhao, X.; Liu, M.; Wee, A. T. S. *ACS Nano* **2021**, *15*, 2165−2181.
(71) Martins Ferreira, E. H.; Moutinho, M. V. O.; Stavale, F.; Lucchese, M. M.; Capaz, R. B.; Achete, C. A.; Jorio, A. *Phys. Rev. B* **2010**, *82*, 125429.
(72) Mignuzzi, S.; Pollard, A. J.; Bonini, N.; Brennan, B.; Gilmore, I. S.; Pimenta, M. A.; Richards, D.; Roy, D. *Phys. Rev. B* **2015**, *91*, 195411.
(73) Shi, W.; Lin, M.-L.; Tan, Q.-H.; Qiao, X.-F.; Zhang, J.; Tan, P.-H. *2D Mater.* **2016**, *3*, No. 025016.
(74) Lin, T.; Cong, X.; Lin, M.-L.; Liu, X.-L.; Tan, P.-H. *Nanoscale* **2018**, *10*, 8704−8711.
(75) Lucchese, M.; Stavale, F.; Ferreira, E. M.; Vilani, C.; Moutinho, M.; Capaz, R. B.; Achete, C.; Jorio, A. *Carbon* **2010**, *48*, 1592−1597.
(76) Gustavo Cançado, L.; Gomes da Silva, M.; Martins Ferreira, E. H.; Hof, F.; Kampioti, K.; Huang, K.; Pénicaud, A.; Alberto Achete, C.; Capaz, R. B.; Jorio, A. *2D Mater.* **2017**, *4*, No. 025039.
(77) Richter, H.; Wang, Z. P.; Ley, L. *Solid State Commun.* **1981**, *39*, 625−629.
(78) Malard, L.; Pimenta, M.; Dresselhaus, G.; Dresselhaus, M. *Phys. Rep.* **2009**, *473*, 51−87.
(79) Thomsen, C.; Reich, S. *Phys. Rev. Lett.* **2000**, *85*, 5214−5217.
(80) Stadler, J.; Schmid, T.; Zenobi, R. *ACS Nano* **2011**, *5*, 8442−8448.
(81) Su, W.; Roy, D. *J. Vac. Sci. Technol. B* **2013**, *31*, No. 041808.
(82) Su, W.; Kumar, N.; Dai, N.; Roy, D. *Chem. Commun.* **2016**, *52*, 8227−8230.
(83) Kato, R.; Umakoshi, T.; Sam, R. T.; Verma, P. *Appl. Phys. Lett.* **2019**, *114*, No. 073105.
(84) Zhang, W.; Wang, Q.; Chen, Y.; Wang, Z.; Wee, A. T. S. *2D Mater.* **2016**, *3*, No. 022001.
(85) Shi, Z.; Wang, X.; Sun, Y.; Li, Y.; Zhang, L. *Semicond. Sci. Technol.* **2018**, *33*, No. 093001.
(86) Wu, X.; Chen, X.; Yang, R.; Zhan, J.; Ren, Y.; Li, K. *Small* **2022**, *18*, 2105877.
(87) Pei, S.; Wang, Z.; Xia, J. *ACS Nano* **2022**, *16*, 11498−11503.
(88) Wu, J.-B.; Zhang, X.; Ijäs, M.; Han, W.-P.; Qiao, X.-F.; Li, X.-L.; Jiang, D.-S.; Ferrari, A. C.; Tan, P.-H. *Nat. Commun.* **2014**, *5*, 5309.

https://doi.org/10.1021/acs.analchem.3c00272
Anal. Chem. 2023, 95, 10821−10838

(89) Wu, J.-B.; Wang, H.; Li, X.-L.; Peng, H.; Tan, P.-H. *Carbon* **2016**, *110*, 225−231.
(90) Lee, J.-U.; Kim, K.; Cheong, H. *2D Mater.* **2015**, *2*, No. 044003.
(91) Tan, Q.-H.; Sun, Y.-J.; Liu, X.-L.; Zhao, Y.; Xiong, Q.; Tan, P.-H.; Zhang, J. *2D Mater.* **2017**, *4*, No. 031007.
(92) Kim, S.; Kim, K.; Lee, J.-U.; Cheong, H. *2D Mater.* **2017**, *4*, No. 045002.
(93) Lin, M.-L.; Zhou, Y.; Wu, J.-B.; Cong, X.; Liu, X.-L.; Zhang, J.; Li, H.; Yao, W.; Tan, P.-H. *Nat. Commun.* **2019**, *10*, 2419.
(94) Nguyen, M. H.; Lim, S. Y.; Taniguchi, T.; Wantanabe, K.; Cheong, H. *2D Mater.* **2021**, *8*, No. 045004.
(95) Wu, H.; Lin, M.-L.; Leng, Y.-C.; Chen, X.; Zhou, Y.; Zhang, J.; Tan, P.-H. *npj 2D Mater. Appl.* **2022**, *6*, 87.
(96) Zhang, X.; Han, W.-P.; Qiao, X.-F.; Tan, Q.-H.; Wang, Y.-F.; Zhang, J.; Tan, P.-H. *Carbon* **2016**, *99*, 118−122.
(97) Lu, X.; Utama, M. I. B.; Lin, J.; Luo, X.; Zhao, Y.; Zhang, J.; Pantelides, S. T.; Zhou, W.; Quek, S. Y.; Xiong, Q. *Adv. Mater.* **2015**, *27*, 4502−4508.
(98) Luo, X.; Lu, X.; Cong, C.; Yu, T.; Xiong, Q.; Ying Quek, S. *Sci. Rep.* **2015**, *5*, 14565.
(99) Liang, L.; Puretzky, A. A.; Sumpter, B. G.; Meunier, V. *Nanoscale* **2017**, *9*, 15340−15355.
(100) Cheon, Y.; Lim, S. Y.; Kim, K.; Cheong, H. *ACS Nano* **2021**, *15*, 2962−2970.
(101) Huang, S.; Liang, L.; Ling, X.; Puretzky, A. A.; Geohegan, D. B.; Sumpter, B. G.; Kong, J.; Meunier, V.; Dresselhaus, M. S. *Nano Lett.* **2016**, *16*, 1435−1444.
(102) Lin, M.-L.; Tan, Q.-H.; Wu, J.-B.; Chen, X.-S.; Wang, J.-H.; Pan, Y.-H.; Zhang, X.; Cong, X.; Zhang, J.; Ji, W.; Hu, P.-A.; Liu, K.-H.; Tan, P.-H. *ACS Nano* **2018**, *12*, 8770−8780.
(103) Quan, J.; Linhart, L.; Lin, M.-L.; Lee, D.; Zhu, J.; Wang, C.-Y.; Hsu, W.-T.; Choi, J.; Embley, J.; Young, C.; Taniguchi, T.; Watanabe, K.; Shih, C.-K.; Lai, K.; MacDonald, A. H.; Tan, P.-H.; Libisch, F.; Li, X. *Nat. Mater.* **2021**, *20*, 1100−1105.
(104) Lui, C. H.; Ye, Z.; Ji, C.; Chiu, K.-C.; Chou, C.-T.; Andersen, T. I.; Means-Shively, C.; Anderson, H.; Wu, J.-M.; Kidd, T.; Lee, Y.-H.; He, R. *Phys. Rev. B* **2015**, *91*, 165403.
(105) Li, H.; Wu, J.-B.; Ran, F.; Lin, M.-L.; Liu, X.-L.; Zhao, Y.; Lu, X.; Xiong, Q.; Zhang, J.; Huang, W.; Zhang, H.; Tan, P.-H. *ACS Nano* **2017**, *11*, 11714−11723.
(106) Zhang, K.; Guo, Y.; Ji, Q.; Lu, A.-Y.; Su, C.; Wang, H.; Puretzky, A. A.; Geohegan, D. B.; Qian, X.; Fang, S.; Kaxiras, E.; Kong, J.; Huang, S. *J. Am. Chem. Soc.* **2020**, *142*, 17499−17507.
(107) Kim, S.; Konar, A.; Hwang, W.-S.; Lee, J. H.; Lee, J.; Yang, J.; Jung, C.; Kim, H.; Yoo, J.-B.; Choi, J.-Y.; Jin, Y. W.; Lee, S. Y.; Jena, D.; Choi, W.; Kim, K. *Nat. Commun.* **2012**, *3*, 1011.
(108) Kaasbjerg, K.; Bhargavi, K. S.; Kubakaddi, S. S. *Phys. Rev. B* **2014**, *90*, 165436.
(109) Ruppert, C.; Chernikov, A.; Hill, H. M.; Rigosi, A. F.; Heinz, T. F. *Nano Lett.* **2017**, *17*, 644−651.
(110) Moody, G.; Kavir Dass, C.; Hao, K.; Chen, C.-H.; Li, L.-J.; Singh, A.; Tran, K.; Clark, G.; Xu, X.; Berghäuser, G.; Malic, E.; Knorr, A.; Li, X. *Nat. Commun.* **2015**, *6*, 8315.
(111) Selig, M.; Berghäuser, G.; Raja, A.; Nagler, P.; Schüller, C.; Heinz, T. F.; Korn, T.; Chernikov, A.; Malic, E.; Knorr, A. *Nat. Commun.* **2016**, *7*, 13279.
(112) Miller, B.; Lindlau, J.; Bommert, M.; Neumann, A.; Yamaguchi, H.; Holleitner, A.; Högele, A.; Wurstbauer, U. *Nat. Commun.* **2019**, *10*, 807.
(113) Carvalho, B. R.; Malard, L. M.; Alves, J. M.; Fantini, C.; Pimenta, M. A. *Phys. Rev. Lett.* **2015**, *114*, 136403.
(114) Ling, X.; Huang, S.; Hasdeo, E. H.; Liang, L.; Parkin, W. M.; Tatsumi, Y.; Nugraha, A. R. T.; Puretzky, A. A.; Das, P. M.; Sumpter, B. G.; Geohegan, D. B.; Kong, J.; Saito, R.; Drndic, M.; Meunier, V.; Dresselhaus, M. S. *Nano Lett.* **2016**, *16*, 2260−2267.
(115) Mao, N.; Wang, X.; Lin, Y.; Sumpter, B. G.; Ji, Q.; Palacios, T.; Huang, S.; Meunier, V.; Dresselhaus, M. S.; Tisdale, W. A.; Liang, L.; Ling, X.; Kong, J. *J. Am. Chem. Soc.* **2019**, *141*, 18994−19001.
(116) Qiu, D. Y.; da Jornada, F. H.; Louie, S. G. *Phys. Rev. Lett.* **2013**, *111*, 216805.
(117) Tran, V.; Soklaski, R.; Liang, Y.; Yang, L. *Phys. Rev. B* **2014**, *89*, 235319.
(118) Aslan, B.; Chenet, D. A.; van der Zande, A. M.; Hone, J. C.; Heinz, T. F. *ACS Photonics* **2016**, *3*, 96−101.
(119) Martin, R. M.; Damen, T. C. *Phys. Rev. Lett.* **1971**, *26*, 86−88.
(120) Drapcho, S. G.; Kim, J.; Hong, X.; Jin, C.; Shi, S.; Tongay, S.; Wu, J.; Wang, F. *Phys. Rev. B* **2017**, *95*, 165417.
(121) Tan, Q.-H.; Sun, Y.-J.; Liu, X.-L.; Xu, K.-X.; Gao, Y.-F.; Ren, S.-L.; Tan, P.-H.; Zhang, J. *Nano Res.* **2021**, *14*, 239−244.
(122) Martin, R. M. *Phys. Rev. B* **1971**, *4*, 3676−3685.
(123) Zhao, Y.; Zhang, S.; Shi, Y.; Zhang, Y.; Saito, R.; Zhang, J.; Tong, L. *ACS Nano* **2020**, *14*, 10527−10535.
(124) Zhao, Y.; Han, S.; Zhang, J.; Tong, L. *J. Raman Spectrosc.* **2021**, *52*, 525−531.
(125) Jin, C.; Kim, J.; Suh, J.; Shi, Z.; Chen, B.; Fan, X.; Kam, M.; Watanabe, K.; Taniguchi, T.; Tongay, S.; Zettl, A.; Wu, J.; Wang, F. *Nat. Phys.* **2017**, *13*, 127−131.
(126) Chow, C. M.; Yu, H.; Jones, A. M.; Yan, J.; Mandrus, D. G.; Taniguchi, T.; Watanabe, K.; Yao, W.; Xu, X. *Nano Lett.* **2017**, *17*, 1194−1199.
(127) Song, C.; Fan, F.; Xuan, N.; Huang, S.; Wang, C.; Zhang, G.; Wang, F.; Xing, Q.; Lei, Y.; Sun, Z.; Wu, H.; Yan, H. *Phys. Rev. B* **2019**, *99*, 195414.
(128) Li, L.; Schultz, J. F.; Mahapatra, S.; Liu, X.; Shaw, C.; Zhang, X.; Hersam, M. C.; Jiang, N. *J. Am. Chem. Soc.* **2021**, *143*, 15624−15634.
(129) Blundo, E.; Cappelluti, E.; Felici, M.; Pettinari, G.; Polimeni, A. *Appl. Phys. Rev.* **2021**, *8*, No. 021318.
(130) Mohiuddin, T. M. G.; Lombardo, A.; Nair, R. R.; Bonetti, A.; Savini, G.; Jalil, R.; Bonini, N.; Basko, D. M.; Galiotis, C.; Marzari, N.; Novoselov, K. S.; Geim, A. K.; Ferrari, A. C. *Phys. Rev. B* **2009**, *79*, 205433.
(131) Huang, M.; Yan, H.; Chen, C.; Song, D.; Heinz, T. F.; Hone, J. *Proc. Natl. Acad. Sci. U. S. A.* **2009**, *106*, 7304−7308.
(132) Conley, H. J.; Wang, B.; Ziegler, J. I.; Haglund, R. F.; Pantelides, S. T.; Bolotin, K. I. *Nano Lett.* **2013**, *13*, 3626−3630.
(133) Rice, C.; Young, R. J.; Zan, R.; Bangert, U.; Wolverson, D.; Georgiou, T.; Jalil, R.; Novoselov, K. S. *Phys. Rev. B* **2013**, *87*, No. 081307.
(134) Fei, R.; Yang, L. *Appl. Phys. Lett.* **2014**, *105*, No. 083120.
(135) Li, Y.; Hu, Z.; Lin, S.; Lai, S. K.; Ji, W.; Lau, S. P. *Adv. Funct. Mater.* **2017**, *27*, 1600986.
(136) Lee, J.-U.; Woo, S.; Park, J.; Park, H. C.; Son, Y.-W.; Cheong, H. *Nat. Commun.* **2017**, *8*, 1370.
(137) Zhao, W.; Tan, P. H.; Liu, J.; Ferrari, A. C. *J. Am. Chem. Soc.* **2011**, *133*, 5941−5946.
(138) Chen, C.-F.; Park, C.-H.; Boudouris, B. W.; Horng, J.; Geng, B.; Girit, C.; Zettl, A.; Crommie, M. F.; Segalman, R. A.; Louie, S. G.; Wang, F. *Nature* **2011**, *471*, 617−620.
(139) Wang, Y.; Xiao, J.; Zhu, H.; Li, Y.; Alsaid, Y.; Fong, K. Y.; Zhou, Y.; Wang, S.; Shi, W.; Wang, Y.; Zettl, A.; Reed, E. J.; Zhang, X. *Nature* **2017**, *550*, 487−491.
(140) Wang, G.; Li, X.; Wang, Y.; Zheng, Z.; Dai, Z.; Qi, X.; Liu, L.; Cheng, Z.; Xu, Z.; Tan, P.; Zhang, Z. *J. Phys. Chem. C* **2017**, *121*, 26034−26043.
(141) Zhang, X.; Zhu, T.; Huang, J.; Wang, Q.; Cong, X.; Bi, X.; Tang, M.; Zhang, C.; Zhou, L.; Zhang, D.; Su, T.; Dai, X.; Meng, K.; Li, Z.; Qiu, C.; Zhao, W.-W.; Tan, P.-H.; Zhang, H.; Yuan, H. *ACS Appl. Mater. Interfaces* **2020**, *12*, 46900−46907.
(142) Das, A.; Pisana, S.; Chakraborty, B.; Piscanec, S.; Saha, S. K.; Waghmare, U. V.; Novoselov, K. S.; Krishnamurthy, H. R.; Geim, A. K.; Ferrari, A. C.; Sood, A. K. *Nat. Nanotechnol.* **2008**, *3*, 210−215.
(143) Lazzeri, M.; Piscanec, S.; Mauri, F.; Ferrari, A. C.; Robertson, J. *Phys. Rev. B* **2006**, *73*, 155426.
(144) Bonini, N.; Lazzeri, M.; Marzari, N.; Mauri, F. *Phys. Rev. Lett.* **2007**, *99*, 176802.

https://doi.org/10.1021/acs.analchem.3c00272
Anal. Chem. 2023, 95, 10821−10838

(145) Chakraborty, B.; Bera, A.; Muthu, D. V. S.; Bhowmick, S.; Waghmare, U. V.; Sood, A. K. *Phys. Rev. B* **2012**, *85*, 161403.
(146) Chakraborty, B.; Gupta, S. N.; Singh, A.; Kuiri, M.; Kumar, C.; Muthu, D. V. S.; Das, A.; Waghmare, U. V.; Sood, A. K. *2D Mater.* **2016**, *3*, No. 015008.
(147) Frey, G. L.; Tenne, R.; Matthews, M. J.; Dresselhaus, M. S.; Dresselhaus, G. *Phys. Rev. B* **1999**, *60*, 2883−2892.
(148) Peimyoo, N.; Yang, W.; Shang, J.; Shen, X.; Wang, Y.; Yu, T. *ACS Nano* **2014**, *8*, 11320−11329.
(149) Kang, D.-H.; Shim, J.; Jang, S. K.; Jeon, J.; Jeon, M. H.; Yeom, G. Y.; Jung, W.-S.; Jang, Y. H.; Lee, S.; Park, J.-H. *ACS Nano* **2015**, *9*, 1099−1107.
(150) Yan, J.; Zhang, Y.; Kim, P.; Pinczuk, A. *Phys. Rev. Lett.* **2007**, *98*, 166802.
(151) Piscanec, S.; Lazzeri, M.; Mauri, F.; Ferrari, A. C.; Robertson, J. *Phys. Rev. Lett.* **2004**, *93*, 185503.
(152) Chen, X.; Reichardt, S.; Lin, M.-L.; Leng, Y.-C.; Lu, Y.; Wu, H.; Mei, R.; Wirtz, L.; Zhang, X.; Ferrari, A. C.; Tan, P.-H. *ACS Nano* **2023**, *17*, 5956−5962.
(153) Zakhidov, D.; Rehn, D. A.; Reed, E. J.; Salleo, A. *ACS Nano* **2020**, *14*, 2894−2903.
(154) Dhakal, K. P.; Ghimire, G.; Chung, K.; Duong, D. L.; Kim, S. W.; Kim, J. *ACS Nano* **2019**, *13*, 14437−14446.
(155) Mai, T. T.; Garrity, K. F.; McCreary, A.; Argo, J.; Simpson, J. R.; Doan-Nguyen, V.; Aguilar, R. V.; Walker, A. R. H. *Sci. Adv.* **2021**, *7*, No. eabj3106.
(156) Choe, J.; Lujan, D.; Rodriguez-Vega, M.; Ye, Z.; Leonardo, A.; Quan, J.; Nunley, T. N.; Chang, L.-J.; Lee, S.-F.; Yan, J.; Fiete, G. A.; He, R.; Li, X. *Nano Lett.* **2021**, *21*, 6139−6145.
(157) Padmanabhan, H.; Poore, M.; Kim, P. K.; Koocher, N. Z.; Stoica, V. A.; Puggioni, D.; Wang, H.; Shen, X.; Reid, A. H.; Gu, M.; Wetherington, M.; Lee, S. H.; Schaller, R. D.; Mao, Z.; Lindenberg, A. M.; Wang, X.; Rondinelli, J. M.; Averitt, R. D.; Gopalan, V. *Nat. Commun.* **2022**, *13*, 1929.
(158) Sun, Y.-J.; Lai, J.-M.; Pang, S.-M.; Liu, X.-L.; Tan, P.-H.; Zhang, J. *J. Phys. Chem. Lett.* **2022**, *13*, 1533−1539.
(159) Gadelha, A. C.; Ohlberg, D. A. A.; Rabelo, C.; Neto, E. G. S.; Vasconcelos, T. L.; Campos, J. L.; Lemos, J. S.; Ornelas, V.; Miranda, D.; Nadas, R.; Santana, F. C.; Watanabe, K.; Taniguchi, T.; van Troeye, B.; Lamparski, M.; Meunier, V.; Nguyen, V.-H.; Paszko, D.; Charlier, J.-C.; Campos, L. C.; et al. *Nature* **2021**, *590*, 405−409.

https://doi.org/10.1021/acs.analchem.3c00272
Anal. Chem. 2023, 95, 10821−10838